Soil Dynamics and Earthquake Engineering 203 (2026) 110136

Contents lists available at ScienceDirect

Soil Dynamics and Earthquake Engineering

journal homepage: www.elsevier.com/locate/soildyn

A novel bedrock power spectral model incorporating seismic magnitude-distance effects for structural reliability analysis and safety assessment

Dengke Jiu [a,b], Yan-Gang Zhao [a,b], Haizhong Zhang [c,*]

[a] College of Architecture and Civil Engineering, Beijing University of Technology, Beijing, 100124, China
[b] Key Laboratory of Urban Security and Disaster Engineering of Ministry of Education, Beijing University of Technology, Beijing, 100124, China
[c] Eco-Science Course, Faculty of Agriculture, Yamagata University, 1-23, Wakaba-machi, Tsuruoka-shi, Yamagata, 997-8555, Japan

ARTICLE INFO

Keywords:
Structural reliability analysis
Structural safe assessment
Seismic ground motions
Bedrock power spectral model
Magnitude
Distance

ABSTRACT

Power spectral density models are used to characterize the frequency-domain properties of seismic ground motions and are widely applied in structural reliability analysis and safety assessment. Existing power spectral models are typically categorized as stationary and nonstationary based on the temporal variability of seismic excitations, which are commonly employed to generate synthetic seismic waves for structural dynamic analysis randomly. However, most existing models assume the bedrock seismic motions as white-noise processes and do not consider the influence of earthquake magnitude and distance on amplitude and spectral content. This can introduce bias into the characterization of the energy distribution, thereby reducing the accuracy of structural response prediction and failure-probability assessment. To address these limitations, this study proposes a bedrock power spectral density model that explicitly incorporates earthquake magnitude and distance, and reveals their physical influence mechanisms. The model is developed based on the comprehensive statistical analysis of seismic records from two datasets, which quantifies the effects of earthquake magnitude and distance on power spectral characteristics. To validate the proposed model, synthetic seismic motions are generated and used to compute the seismic responses and failure probabilities of a case-study structure, providing quantitative evidence for transitioning seismic input modeling from a "single-assumption" paradigm to a magnitude-distance-conditioned characterization. Overall, the proposed model introduces an interpretable magnitude-distance modulation mechanism into bedrock frequency-domain modeling, providing a more targeted representation of seismic input for structural reliability analysis and seismic safety assessment.

1. Introduction

Seismic ground motions exhibit significant randomness and uncertainty, and accurately characterizing and simulating such stochastic motions has become a core challenge in the field of structural engineering, particularly in seismic reliability analysis and safe assessment [1–3]. Over the past several decades, extensive research has been conducted in stochastic dynamic analysis focusing on the modeling and simulation of seismic motions, aiming to precisely predict structural responses under seismic excitations [4,5]. Among various characterization methods, power spectral models serve as key tools for representing the frequency-domain features of seismic motions, effectively capturing their frequency distribution characteristics [6,7]. These models not only provide critical support for stochastic structural dynamic analysis but also constitute fundamental components in structural reliability analysis and safety assessment [8]. Accurate seismic ground motion power spectral inputs are of vital importance for promoting scientific seismic design and risk evaluation [9].

Over the past several decades, numerous models for the power spectrum of seismic ground motions have been developed, which can be classified into stationary and nonstationary types according to their statistical characteristics [10]. For earthquakes with relatively distant sources and stable statistical properties, stationary models have been widely adopted to simulate ground motions. Most existing formulations are improved based on the classical Kanai-Tajimi model [11,12], which assumes bedrock motion as white noise and derives the surface power

---

* Corresponding author.
E-mail address: zhang@tds1.tr.yamagata-u.ac.jp (H. Zhang).

https://doi.org/10.1016/j.soildyn.2026.110136
Received 14 November 2025; Received in revised form 31 December 2025; Accepted 17 January 2026

spectrum through transmission by the overlying soil layers. However, since the model exhibits the zero component at zero frequency in the low-frequency range and fails to converge in high-frequency energy, many researchers have proposed improvements targeting its low-frequency, high-frequency, and overall spectral characteristics. Overall, these improvements can be classified into four categories: The first category is low-frequency correction models, which aim to address the problem that the Kanai–Tajimi spectrum fails to approach zero as the frequency tends to zero, leading to overestimation of long-period components. Such improved models typically introduce empirical correction terms or apply single-degree-of-freedom (SDOF) oscillator filters, as represented by the Hu model, the Hong model, the Peng model, and the Clough-Penzien models [13,14]. The second category is high-frequency correction models, which focus on maintaining finite spectral amplitudes in the high-frequency range by incorporating high-frequency correction terms to prevent unbounded growth, with the Ou model [14] as a representative example. The third category is simultaneous low- and high-frequency correction models, which introduce dual correction terms to adjust both low- and high-frequency components, ensuring that the model approaches zero in both the low- and high-frequency ranges, such as the Du and Li models [15]. The fourth category is multiple filtering models, which apply two or more rounds of filtering to the bedrock motion to produce multi-peaked spectra, thereby better reproducing the multiple spectral peaks often observed in actual earthquake ground motions, as exemplified by the Lai model [16].

Although these models have been widely applied in structural reliability analysis, they often fail to accurately capture the time-varying characteristics of ground motions during strong earthquakes, near-fault events, or motions with pronounced short-term variations [17–19]. In such cases, the stochastic evolutionary power spectral density (EPSD) model is typically used to characterize these seismic motions [20]. Two well-known approaches for estimating the EPSD function were suggested in the literature. One was proposed by Priestley and the other was proposed by Spanos and Failla [19]. In the approach proposed by Priestley [21], the EPSD function for a given sample or time-varying signal of a stochastic process is estimated by first applying the short-time Fourier transform (STFT) to decompose the signal and to obtain the time-frequency dependent power distribution. The approach proposed by Spanos and Failla [22] was formulated by directly applying the continuous wavelet transform (CWT) to the evolutionary process and considering that the amplitude modulation function is slowly varying. Additionally, Vlachos et al. [23] proposed a non-stationary evolutionary bimodal stochastic ground motion model based on the Kanai-Tajimi model. This model can effectively characterize multimodal evolutionary power spectra and more accurately describe the time-varying distribution of spectral energy.

All the aforementioned power spectral models assume bedrock seismic motion as white noise, subsequently applying various filters to modify the power spectrum [24]. According to this white noise assumption, the bedrock power spectrum should remain constant across all frequencies [25]. However, empirical observations and studies indicate that both the frequency content and amplitude of bedrock seismic motions are significantly influenced by seismic magnitude and distance [16,26]. These influences reflect the attenuation and frequency-dependent characteristics of seismic waves during propagation, which directly affect the dynamic input and response of structures [27,28]. In response to this limitation, many studies have bypassed the basic form of classical power spectral models and proposed ground-motion surface spectral models that account for magnitude and distance based on observed seismic records. Vlachos et al. [29] developed a predictive model for specific regions using statistical regression, incorporating site parameters such as magnitude and distance. Similarly, Bayless et al. [30] developed an effective Fourier amplitude spectrum model for California, considering magnitude and distance to improve site-specific spectral predictions. To enable direct generation of ground motions for structural reliability analysis, Wang et al. [31] proposed a nonstationary evolutionary power spectral model that accounts for magnitude and distance, addressing both source parameter effects and the requirements for synthetic wave generation. A limitation of this model is that it relies on the conversion between Fourier spectra and power spectra, thereby neglecting the influence of strong-motion duration. Furthermore, Ding et al. [32] developed a power spectral model framework based on machine learning, which considers magnitude and distance, significantly improving prediction accuracy. However, these models still consider seismic parameters such as magnitude and distance only at the level of regional applicability or data fitting, without systematically analyzing the physical mechanisms by which magnitude and distance influence seismic spectral characteristics, nor providing a generalizable power spectral model that can be directly applied to structural reliability analysis while maintaining both physical interpretability and waveform generation capability.

To address this issue, this study proposes a bedrock power spectral model that explicitly incorporates the effects of seismic magnitude and distance. On one hand, the model integrates physical principles with empirical regression, providing an in-depth interpretation of the influence mechanisms of magnitude and distance on spectral characteristics, including amplitude, bandwidth, and attenuation behavior. On the other hand, the model can directly replace the constant white-noise values used in classical models, maintaining a concise formulation while facilitating the generation of ground motions for structural reliability analysis. The main contributions of this study are as follows:

1. Highlighted the frequency components of the bedrock power spectrum vary significantly with seismic magnitude and distance, indicating that the bedrock seismic motion power spectrum is not constant across all frequencies. This challenges the conventional assumption in existing power spectral models that treat bedrock seismic motions as white noise processes.
2. Systematically analyzed the power spectral results and assessed the physical mechanisms by which magnitude and distance influence spectral characteristics based on a large dataset of bedrock ground motions. Specifically, magnitude primarily governs the amplitude and bandwidth, and distance controls the high-frequency attenuation of the spectrum.
3. Calculated the surface power spectra considering the effects of magnitude and distance by integrating the proposed model with the Kanai-Tajimi model, which not only effectively incorporates the influences of magnitude and distance but also strictly satisfies the physical constraints of zero-frequency nullity and finite energy in the bedrock power spectrum, thereby enhancing the accuracy and physical consistency of power spectral modeling.
4. Applied the proposed model in structural seismic response and failure probability calculations, enabling the prediction of stochastic responses for any magnitude–distance combination. It addresses the issue of overly conservative designs that may result from traditional models relying on a single input. While ensuring structural safety, the model provides a more scientifically grounded and economically efficient framework for structural reliability analysis.

The remainder of this paper is organized as follows. Section 2 provides a comprehensive review of existing power spectral models. Section 3 introduces an extensive dataset of bedrock seismic records used to develop a model incorporating the effects of magnitude and distance. In Section 4, a novel bedrock power spectral model that considers the effects of magnitude and distance is proposed and validated based on analysis of seismic records, and it is then used to conduct structural reliability analyses for different magnitude–distance classifications. Finally, the conclusions are presented in Section 5.

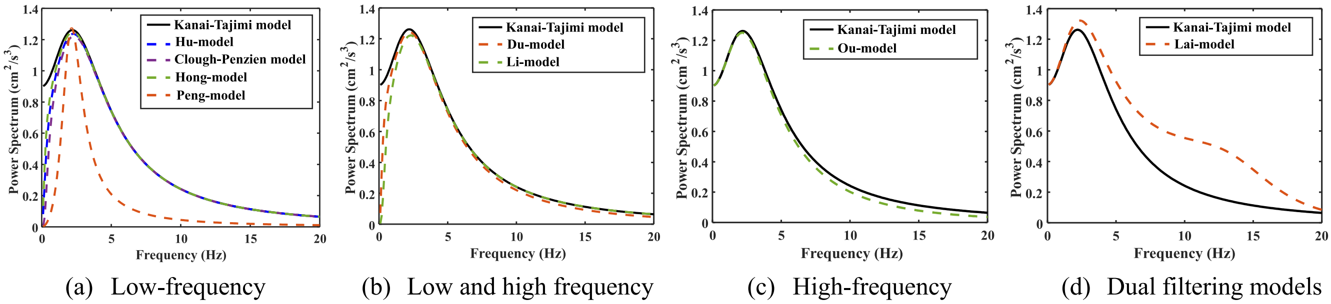

(a) Low-frequency (b) Low and high frequency (c) High-frequency (d) Dual filtering models

Fig. 1. Comparison diagram of existing power spectral models.

2. Review of existing power spectral models

Based on different approaches to characterizing the frequency features of seismic ground motions, existing power spectral models can be broadly classified into stationary and non-stationary categories [32]. Stationary models primarily describe the long-term average spectral characteristics of seismic motions and apply to cases where the seismic source is relatively distant, and the statistical properties of the ground motions are relatively stable [33]. These models effectively capture the overall energy distribution and average frequency components. In contrast, non-stationary power spectral models focus on seismic motions with significant temporal variability, such as strong earthquakes and near-field seismic events, emphasizing the dynamic evolution of the seismic spectrum over time [34]. These models provide a more realistic representation of the instantaneous features and energy concentration variations of seismic motions. In this section, Section 2.1 focuses on widely applied stationary power spectral models, while Section 2.2 systematically reviews recent advances in non-stationary power spectral modeling.

2.1. Stationary power spectral models

This section provides a concise review of the existing power spectral models. The first power spectral model was proposed, in which the seismic motion is assumed to be white noise with a constant power spectral value across all frequencies. This power spectral model, $S(\omega)$, is expressed as follow:

$$S(\omega) = S_0 \quad -\infty < \omega < \infty \tag{1}$$

where ω is the circular frequency of the seismic motion with the unit rad/s; S_0 is a factor used to reflect the intensity of the power spectrum. This model is very simple, requiring only one parameter, i.e., the spectral intensity factor S_0. However, the energy derived from this model is infinite, which does not align with real-world conditions.

Subsequently, several enhanced power spectral models were developed based on the white noise model. In 1960, Kanai and Tajimi [11,12] proposed a power spectral model that assumes the bedrock seismic motion as white noise and then transmitted through the surface soil layer. This model treats the soil layer as a linear SDOF oscillator and can be expressed as follows:

$$S(\omega) = \frac{4{\zeta_g}^2\omega^2{\omega_g}^2 + {\omega_g}^4}{4{\zeta_g}^2\omega^2{\omega_g}^2 + \left({\omega_g}^2\text{-}\omega^2\right)^2} S_0 \tag{2}$$

where ζ_g is the damping ratio of the surface soil layer; ω_g is the fundamental frequency, which can reflect the hardness of the surface soil layer. The Kanai-Tajimi model incorporates the influence of surface soil layers. However, the result of this model is not equal to zero when the frequency approaches zero, which contradicts the rule that the power spectrum should approach zero as frequency approaches zero. This means that this model has a zero-frequency component, as shown by the black curve in Fig. 1(a), and excessively exaggerates the low-frequency components.

To solve the problem of zero-frequency component existing in the Kanai-Tajimi model, the Hu model was proposed to modify the low-frequency components by incorporating a low-frequency correction term $\frac{\omega^2}{\omega^2+\gamma^2}$. The expression of Hu model is as follow:

$$S(\omega) = \frac{4{\zeta_g}^2\omega^2{\omega_g}^2 + {\omega_g}^4}{4{\zeta_g}^2\omega^2{\omega_g}^2 + \left({\omega_g}^2\text{-}\omega^2\right)^2} \frac{\omega^2}{\omega^2 + \gamma^2} S_0 \tag{3}$$

where γ is the low-frequency reduction parameter and is generally set to 2.0 rad/s. The calculation result of this model approaches zero infinitely with the frequency decreasing to zero, as shown by the red dashed line in Fig. 1(a). In the high-frequency range, the prediction results of this model closely align with those of the Kanai-Tajimi model.

Similarly, the Hong model was proposed by incorporating a low-frequency correction term $\frac{\omega^2}{\omega^2+{\omega_c}^2}$ into the Kanai-Tajimi model. The expression is as follow:

$$S(\omega) = \frac{4{\zeta_g}^2\omega^2{\omega_g}^2 + {\omega_g}^4}{4{\zeta_g}^2\omega^2{\omega_g}^2 + \left({\omega_g}^2\text{-}\omega^2\right)^2} \frac{\omega^2}{\omega^2 + {\omega_c}^2} S_0 \tag{4}$$

where ω_c is the low-frequency correction coefficient, and the recommended value is 1.503 rad/s. The Hong model can obtain a result of zero at zero frequency, as indicated by the green dashed line in Fig. 1(a).

Unlike the Hu model and Hong model, Clough and Penzien reduced the low-frequency components by further filtering the Kanai-Tajimi model using a SDOF transfer function $\frac{\omega^4}{4{\zeta_f}^2\omega^2{\omega_f}^2+\left({\omega_f}^2\text{-}\omega^2\right)^2}$. The expression of this model is as follow:

$$S(\omega) = \frac{4{\zeta_g}^2\omega^2{\omega_g}^2 + {\omega_g}^4}{4{\zeta_g}^2\omega^2{\omega_g}^2 + \left({\omega_g}^2\text{-}\omega^2\right)^2} \frac{\omega^4}{4{\zeta_f}^2\omega^2{\omega_f}^2 + \left({\omega_f}^2\text{-}\omega^2\right)^2} S_0 \tag{5}$$

where ω_f is the fundamental frequency, ζ_f is the damping ratio. According to Ref. [8], ω_f = 0.1-0.2ω_g, $\zeta_f = \zeta_g$. The result of the Clough-Penzien model is equal to zero when the frequency approaches zero, as shown by the blue dashed line in Fig. 1(a).

To simplify the above models (Eqs. (2)–(4)) and make the spectral value zero when the frequency approaches zero, Peng adjusted the SDOF transfer function representing the surface soil layer in the Kanai-Tajimi model. Then the Peng model is as follows:

$$S(\omega) = \frac{\omega^2{\omega_g}^2}{4{\zeta_g}^2\omega^2{\omega_g}^2 + \left({\omega_g}^2\text{-}\omega^2\right)^2} S_0 \tag{6}$$

where ζ_g is the damping ratio, ω_g is the fundamental frequency. To make the spectral value zero when the frequency approaches zero, this model removes a term from the numerator of the Kanai-Tajimi model. Compared with other models that only modify low-frequency components, the Peng model approaches zero quickly in both low-frequency and high-frequency ranges, as shown by the orange dashed line in

Fig. 1(a).

The aforementioned models achieve a spectral result of zero at zero frequency by adjusting the low-frequency components. However, many scholars have pointed out that, in addition to meeting the requirement of having no zero-frequency component, the power spectrum should also remain finite in the high-frequency [24]. This means that the variance of the seismic acceleration process, σ^2, should be a finite value:

$$\sigma^2 = \int_0^{\infty} S(\omega)\mathrm{d}\omega \tag{7}$$

To address this issue, the Ou model was proposed that modified the high-frequency components of the Kanai-Tajimi model by incorporating an additional term $\frac{\omega_c^2}{\omega^2+\omega_c^2}$. The Ou model can be expressed as follows:

$$S(\omega) = \frac{4{\zeta_g}^2\omega^2{\omega_g}^2 + {\omega_g}^4}{4{\zeta_g}^2\omega^2{\omega_g}^2 + \left({\omega_g}^2\text{-}\omega^2\right)^2}\frac{{\omega_c}^2}{\omega^2 + {\omega_c}^2}S_0 \tag{8}$$

where $\omega_c = 8\pi$ rad/s. As shown by the orange dashed line in Fig. 1(c), the attenuation rate of the Ou model in the high-frequency range is faster, while it completely overlaps with the Kanai-Tajimi model in the low-frequency range. This model corrects the high-frequency components of the Kanai-Tajimi model to remain finite in the high-frequency ranges.

In addition, to make both low-frequency and high-frequency components finite, the Du model was proposed by incorporating two correction terms based on the Fourier Amplitude Spectral (FAS) model proposed by Boore [35]. The Du model can be expressed as follows:

$$S(\omega) = \frac{4{\zeta_g}^2\omega^2{\omega_g}^2 + {\omega_g}^4}{4{\zeta_g}^2\omega^2{\omega_g}^2 + \left({\omega_g}^2\text{-}\omega^2\right)^2}\frac{1}{1 + (D\omega)^2}\frac{\omega^4}{\left({\omega_0}^2 + \omega^2\right)^2}S_0 \tag{9}$$

where $\frac{1}{1+(D\omega)^2}$ is the low pass filter with the same role of the correction term incorporated by Ou et al., in which D is a spectral parameter with a range of [0.03,0.04]. $\frac{\omega^4}{({\omega_0}^2+\omega^2)^2}$ is the high pass filter with the same role of the transfer function incorporated in the Clough-Penzien model, ω_0 is the corner low-frequency used to suppresses the low-frequency components. All the parameters in the Du model are derived from a large number of actual seismic records. This model not only achieves a spectral result of zero at zero frequency, but also decays to zero quickly in the high-frequency, meeting the requirement of finite energy, as shown by the orange dashed line in Fig. 1(b).

Similarly, the Li model was also proposed an improved power spectral model that simultaneously meets the requirements of having finite energy and no zero-frequency component. Based on the Clough-Penzien model, this model further modifies the high-frequency components by incorporating a suppression term $\frac{{\omega_k}^4}{({\omega_k}^2+\omega^2)^2}$. This model can be represented as follow:

$$S(\omega) = \frac{4{\zeta_g}^2\omega^2{\omega_g}^2 + {\omega_g}^4}{4{\zeta_g}^2\omega^2{\omega_g}^2 + \left({\omega_g}^2\text{-}\omega^2\right)^2}\frac{\omega^4}{4{\zeta_f}^2\omega^2{\omega_f}^2 + \left({\omega_f}^2\text{-}\omega^2\right)^2}\frac{{\omega_k}^4}{\left({\omega_k}^2 + \omega^2\right)^2}S_0 \tag{10}$$

where ω_k is a spectral parameter and generally set to 2.0 rad/s. The results of this model are shown by the green dashed line in Fig. 1(b). This model obtains a spectral result of zero at zero frequency and remains finite in the high-frequency range with a similar modification method to the Du model.

The power spectral models discussed above result in the power spectrum with only one single peak. However, in fact, the power spectrum can sometimes display two distinct peaks rather than just one. To address this issue, Lai et al. [16] proposed a double filtered white noise power spectral model by introducing the second filter $\frac{4{\zeta_h}^2\omega^2{\omega_h}^2+{\omega_h}^4}{4{\zeta_h}^2\omega^2{\omega_h}^2+({\omega_h}^2\text{-}\omega^2)^2}$ into the Kanai-Tajimi model. This model is as follow:

$$S(\omega) = \frac{4{\zeta_g}^2\omega^2{\omega_g}^2 + {\omega_g}^4}{4{\zeta_g}^2\omega^2{\omega_g}^2 + \left({\omega_g}^2\text{-}\omega^2\right)^2}\frac{4{\zeta_h}^2\omega^2{\omega_h}^2 + {\omega_h}^4}{4{\zeta_h}^2\omega^2{\omega_h}^2 + \left({\omega_h}^2\text{-}\omega^2\right)^2}S_0 \tag{11}$$

where ω_h is the fundamental frequency of the secondary filter with a value of 90 rad/s, ζ_h is the damping ratio of the secondary filter with the value of 0.25. As shown by the green dashed line in Fig. 1(d), the power spectrum of this model has a second peak value. In actual seismic motion analysis, using the Lai model with varying parameter values can yield predictions that align with the characteristics of the corresponding regions. Consequently, compared to other models, this model is better suited to simulate the actual seismic power spectrum, which exhibits two peaks.

Overall, the stationary power spectral models reviewed above can reflect site amplification effects to some extent through parameters such as ω_g and ζ_g. However, these models are generally built on a common assumption that bedrock excitation is a white-noise-driven process with the constant spectral intensity S_0. This assumption does not explicitly capture the systematic dependence of spectral amplitude and shape on earthquake magnitude and distance, and therefore has limited ability to represent the frequency-dependent energy distribution and its time-varying characteristics.

2.2. Non-stationary power spectral models

In engineering practice, strong earthquakes, near-field earthquakes, and seismic motions with significant short-term variations are typically considered as non-stationary random processes [36]. The power spectral frequency contents and amplitudes of these seismic motions vary with time; this time-varying characteristic can be described by the EPSD models [37,38]. These models simulate the growth and attenuation process of seismic motions by incorporating time modulation functions or time-varying parameters. The typical representation of the EPSD model can be expressed as follows:

$$S_a(\omega, t) = S_a(\omega)\cdot g(t) \tag{12}$$

where $S_a(\omega)$ is the stationary power spectral model introduced in Section 2.1; $g(t)$ is the time modulation function, typically a time-varying envelope function. It is primarily used to simulate the growth and attenuation process of ground motion, which mainly includes exponential modulation functions, triangular envelope functions and et al.

Taking the Kanai-Tajimi model as an example, Eq. (12) can be expressed as follows:

$$S(\omega) = \frac{S_0\cdot\left(4{\zeta_g}^2\omega^2{\omega_g}^2 + {\omega_g}^4\right)}{4{\zeta_g}^2\omega^2{\omega_g}^2 + \left({\omega_g}^2\text{-}\omega^2\right)^2}\cdot g(t) \tag{13}$$

In recent years, spectral modeling studies have increasingly emphasized “time-frequency nonstationary”, as exemplified by time-frequency power spectral density (TFPSD) formulations and transform-domain nonstationary spectral estimation methods [39]. These approaches typically rely on time-frequency analysis tools such as the S-transform and CWT to characterize the coupled evolution of energy over time and frequency, enabling the representation of frequency-band evolution and localized energy concentration [40,41]. However, these studies are primarily developed for surface ground motions and focus on the time-frequency energy evolution of surface inputs, without explicitly accounting for the effects of earthquake magnitude and source-to-site distance at the bedrock-motion level.

Overall, existing non-stationary spectral frameworks, whether based on time modulation or time-frequency representations, still rely on the white-noise assumption for bedrock motions. Earthquake magnitude and distance are not explicitly modeled as governing factors of the bedrock power spectral amplitude and shape. Consequently, the physical influence mechanism of earthquake magnitude and distance on bedrock spectral characteristics remains insufficiently characterized,

Table 1
Classification of accelerograms based on magnitude and distance from K-NET and KiK-net.

Distance (km)	Magnitude	Record number	Class number
$10 \leq R < 100$	$4.8 \leq M < 5.8$	650	1
	$5.8 \leq M < 6.8$	316	2
	$6.8 \leq M < 8.2$	86	3
$100 \leq R \leq 200$	$4.8 \leq M < 5.8$	186	4
	$5.8 \leq M < 6.8$	250	5
	$6.8 \leq M < 8.2$	122	6

Table 2
Classification of accelerograms based on magnitude and distance from PEER.

Distance (km)	Magnitude	Record number	Class number
$10 \leq R < 100$	$4.8 \leq M < 5.8$	182	1
	$5.8 \leq M < 6.8$	330	2
	$6.8 \leq M < 8.2$	184	3
$100 \leq R \leq 200$	$4.8 \leq M < 5.8$	278	4
	$5.8 \leq M < 6.8$	262	5
	$6.8 \leq M < 8.2$	212	6

underscoring the need to develop a magnitude-distance-dependent bedrock power spectral model.

3. Database

3.1. Seismic records selection

To develop a bedrock power spectral model that explicitly accounts for the effects of earthquake magnitude and distance, a large number of seismic records were selected from the Strong-Motion Seismograph Networks (K-NET and KiK-net) and the Pacific Earthquake Engineering Research Center (PEER) dataset. To ensure that the selected records closely represent bedrock motion characteristics, all their average shear-wave velocity in the upper 30 m, V_{S30}, is greater than 760 m/s. For the PEER and KiK-net datasets, V_{S30} values can be directly obtained, whereas for K-NET, the PS logging depth is limited to 20 m. For these sites, V_{S30} can be calculated by shear-wave velocity in the upper 20m, V_{S20}, based on the equation proposed by Kanno [42] ($V_{S30} = 1.13V_{S20} + 19.5$). It should be noted that K-NET and KiK-net provide only the Japan Meteorological Agency magnitude, M_j, and the epicentral distance, R_e, while the PEER dataset provides the moment magnitude, M_w, and rupture distance, R_{rup}. Since M_w and R_{rup} are more commonly used in seismic modeling studies, M_j values were converted to M_w using the empirical relationship proposed by Uchide and Imanishi [43], and R_e values were converted to R_{rup} following the method of Thompson and Worden [44], thereby ensuring consistency among all datasets.

To ensure the generality of the dataset, 1610 seismic records were selected from the K-NET and KiK-net datasets, and 1448 records were selected from the PEER dataset. The selected records cover the moment magnitude M_w range of 4.8–8.2 and rupture distance R_{rup} range of 10–200 km. Seismic motions from the two datasets were classified into six categories, as detailed in Tables 1 and 2. Figs. 2 and 3 present the statistical distributions of magnitude and distance, providing a visual overview of the sample characteristics within each category. This classification strategy is designed to systematically analyze bedrock power spectral characteristics under different magnitude and distance conditions. Specifically, the energy distribution of the seismic power spectrum is highly sensitive to variations in earthquake magnitude; even minor differences in magnitude can lead to substantial changes in spectral amplitude. Therefore, the classification of samples into three magnitude categories—small, moderate, and large events—not only helps to avoid the "averaging out" of spectral features that may arise from an overly wide magnitude range in statistical analyses, but also enables a clearer

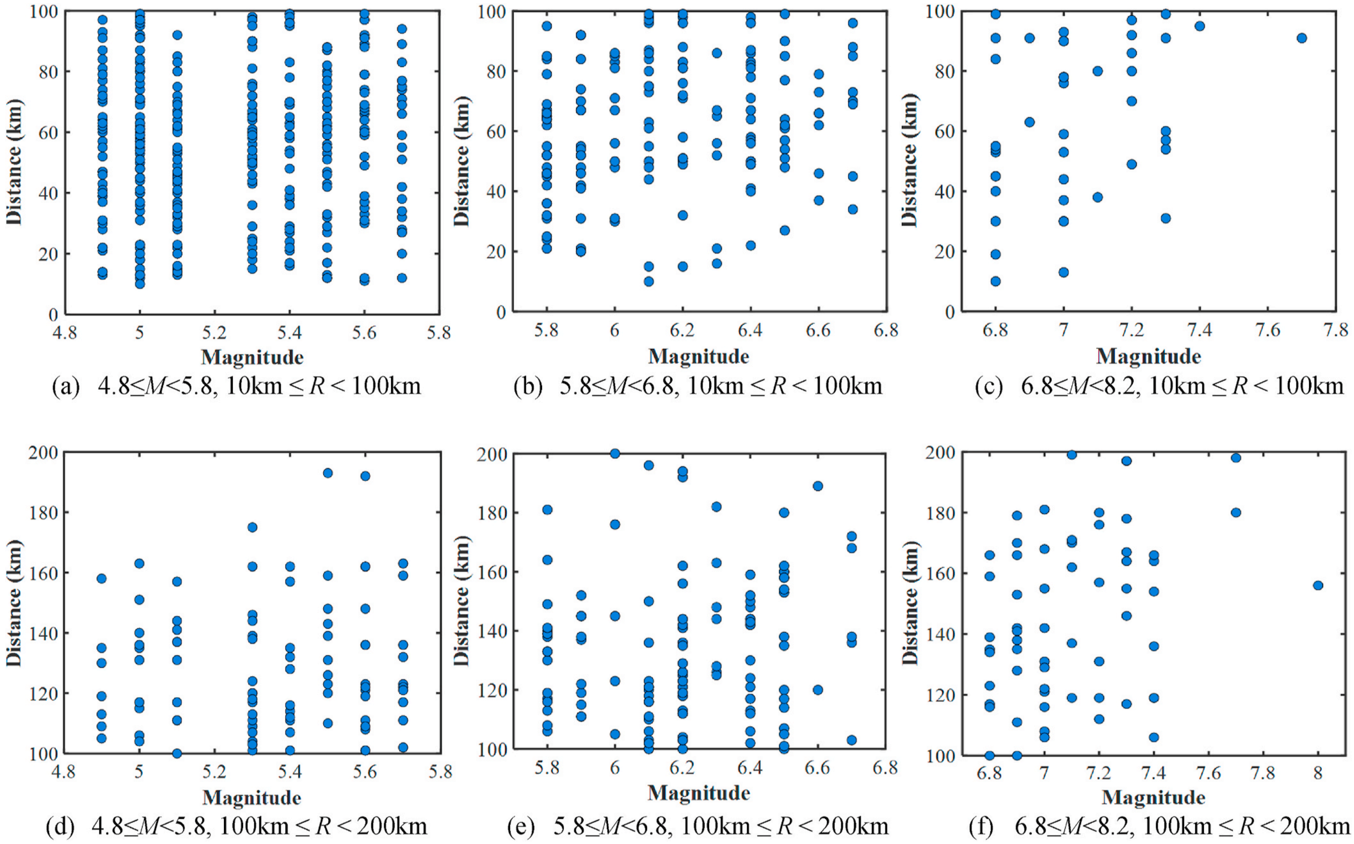

(a) $4.8 \leq M < 5.8$, $10\text{km} \leq R < 100\text{km}$ (b) $5.8 \leq M < 6.8$, $10\text{km} \leq R < 100\text{km}$ (c) $6.8 \leq M < 8.2$, $10\text{km} \leq R < 100\text{km}$

(d) $4.8 \leq M < 5.8$, $100\text{km} \leq R < 200\text{km}$ (e) $5.8 \leq M < 6.8$, $100\text{km} \leq R < 200\text{km}$ (f) $6.8 \leq M < 8.2$, $100\text{km} \leq R < 200\text{km}$

Fig. 2. Distribution of magnitude and distance of 6 classifications from K-NET and KiK-net.

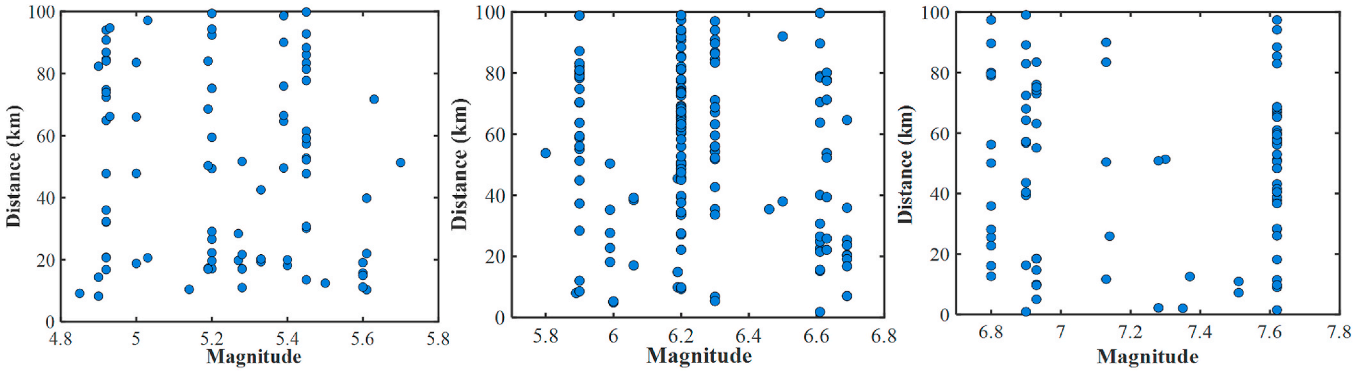

(a) $4.8 \le M < 5.8$, $10\text{km} \le R < 100\text{km}$ (b) $5.8 \le M < 6.8$, $10\text{km} \le R < 100\text{km}$ (c) $6.8 \le M < 8.2$, $10\text{km} \le R < 100\text{km}$

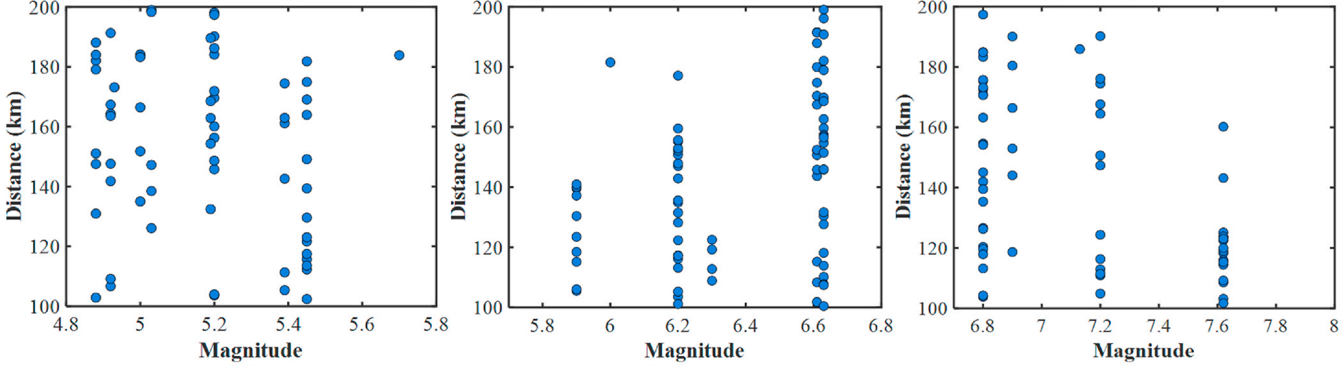

(d) $4.8 \le M < 5.8$, $100\text{km} \le R < 200\text{km}$ (e) $5.8 \le M < 6.8$, $100\text{km} \le R < 200\text{km}$ (f) $6.8 \le M < 8.2$, $100\text{km} \le R < 200\text{km}$

Fig. 3. Distribution of magnitude and distance of 6 classifications from PEER.

examination of how increasing magnitude influences the cross-band energy distribution and overall spectral shape. On the other hand, the distance range was restricted to 10–200 km based on careful considerations of physical rationality and model applicability. This range helps to avoid pulse-like earthquake motions at very short distances ($R < 10$ km), which typically involve complex source-path coupling effects and warrant separate investigation in future studies. At the same time, seismic motions with excessively long distances ($R > 200$ km) are also excluded as their low intensity, which deviates from bedrock characteristics and limits practical relevance for engineering design. In this way, the selected range preserves the fundamental characteristics of bedrock ground motions while maintaining a reasonable balance between energy concentration and propagation attenuation. Furthermore, variations in distance primarily reflect the geometric spreading and energy dissipation of seismic waves along the propagation path. To quantitatively compare the spectral characteristics of near-field and far-field ground motions, a rupture distance of $R_{rup} = 100$km was adopted as an empirical threshold based on the previous research [35,45,46] and actual calculations. The records are classified into two categories: $R_{rup} <$ 100km for energy distribution mechanisms dominated by source effects in the near field and $R_{rup} \geq 100$km for those dominated by path attenuation in the far field, thereby providing a solid basis for the subsequent development of the power spectral model.

3.2. Data preprocessing

Before conducting power spectral analysis, all seismic records were selected in Section. 3.1 underwent systematic data preprocessing to ensure the consistency and accuracy of bedrock power spectral model estimates. The preprocessing primarily included baseline correction,

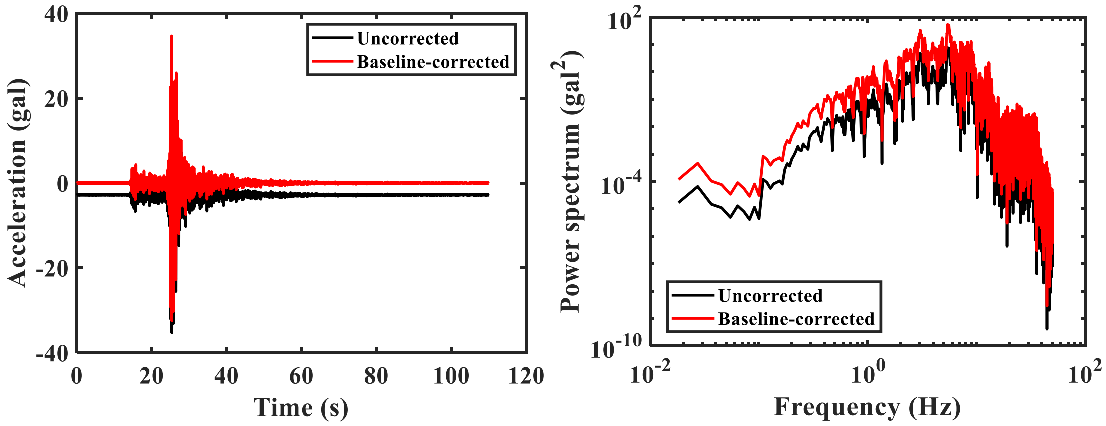

(a) Acceleration comparison (b) Power spectrum comparison

Fig. 4. Comparison of baseline-corrected and uncorrected signal.

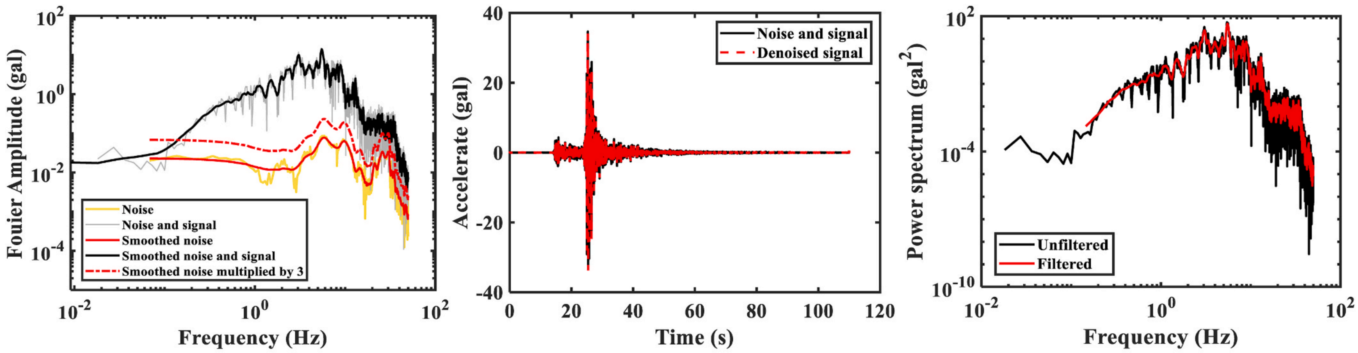

(a) Cutoff frequency selection (b) Noise and denoised signals (c) Filtered and unfiltered power spectrum

Fig. 5. Schematic diagram of noise identification and filtering processing.

noise identification and filtering, and determination of the useable frequency range. First, during the baseline correction stage, a linear baseline correction was applied to each record, which centralizes the data by removing its mean to eliminate distortions caused by instrumental drift or long-term offsets. Fig. 4 illustrates an example record, showing the acceleration time history and corresponding power spectrum before and after baseline correction. It can be observed that the record power spectrum without baseline correction underestimates low-frequency content by approximately 10 %, which would directly affect subsequent model estimation. Therefore, baseline correction can effectively remove the overall shift in the original signal, mitigate systematic bias in the low-frequency range, and thereby improve both the accuracy and physical reliability of the power spectral model estimates.

During the noise identification and filtering stage, the effective seismic motion signals were extracted as follows. First, the pre-event noise window was identified using the automatic P-phase arrival-time picker developed by Kalkan [47], and the Fourier amplitude spectrum (FAS) of the noise was calculated, as indicated by the yellow line in Fig. 5(a). Then, the signal-to-noise ratio (SNR) was computed over the entire frequency range, and frequency bands with SNR <3 were considered unreliable following the method proposed by Bahrampouri et al. [48]. Based on this criterion, the low-frequency cutoff was determined by locating the first intersection between the signal spectrum (black line) and three times the noise spectrum (red dashed line) in Fig. 5 (a), ensuring that power spectral calculations were performed only within high-SNR frequency bands, thereby implementing SNR-based low-frequency filtering. Additionally, to suppress random fluctuations in the high-frequency range, both the signal and noise spectra were smoothed using a moving average, which preserved the main spectral features while producing more continuous and smoother curves. As shown in Fig. 5(c), noise filtering removed the low-frequency signals with excessive noise, retaining only the power spectrum above approximately 0.2 Hz. The smoothing procedure reduced random oscillation amplitudes in the high-frequency range by about 20 %,

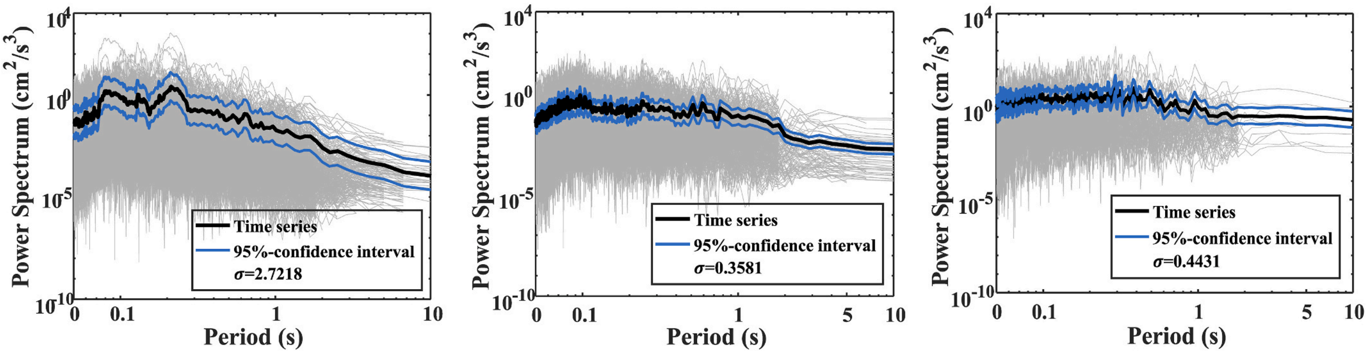

(a) 4.8≤M<5.8, 10km ≤ R < 100km (b) 5.8≤M<6.8, 10km ≤ R < 100km (c) 6.8≤M<8.2, 10km ≤ R < 100km

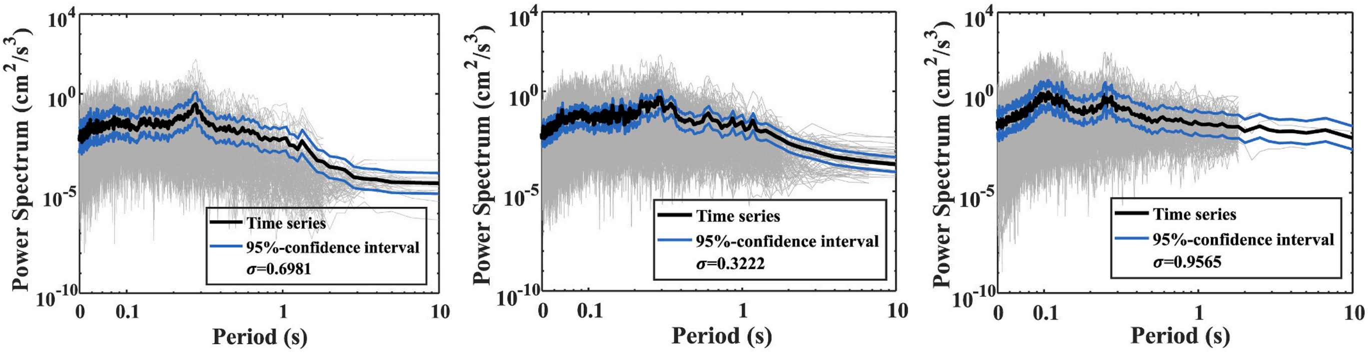

(d) 4.8≤M<5.8, 100km ≤ R < 200km (e) 5.8≤M<6.8, 100km ≤ R < 200km (f) 6.8≤M<8.2, 100km ≤ R < 200km

Fig. 6. Results of recorded bedrock seismic motions of 6 classifications from the K-NET and KiK-net dataset.

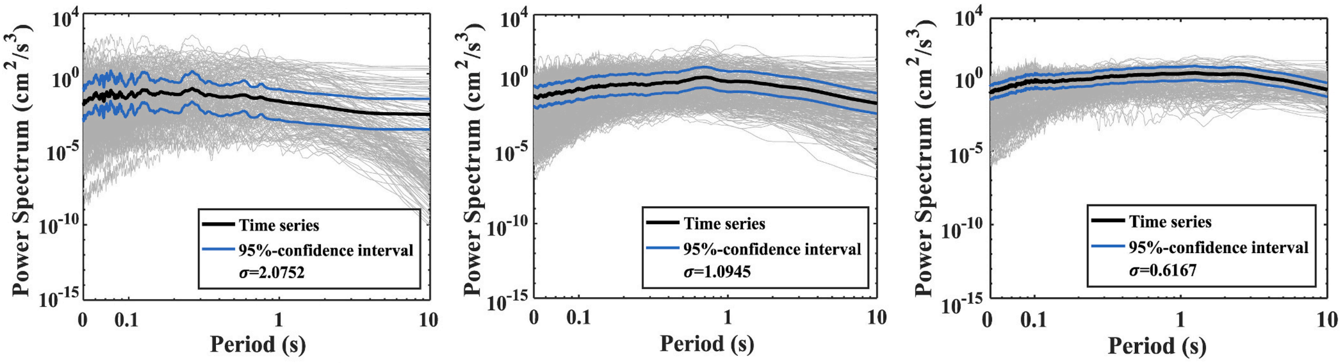

(a) 4.8≤M<5.8, 10km ≤ R < 100km (b) 5.8≤M<6.8, 10km ≤ R < 100km (c) 6.8≤M<8.2, 10km ≤ R < 100km

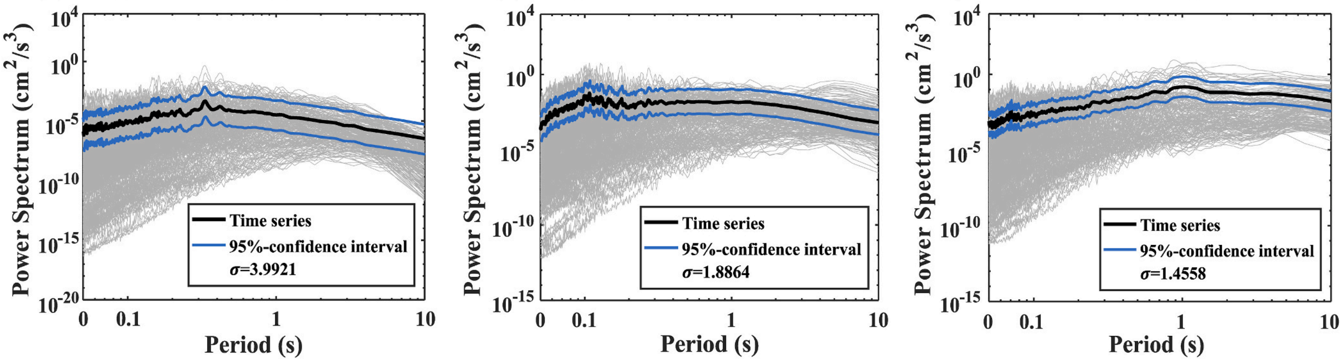

Fig. 7. Results of recorded bedrock seismic motions of 6 classifications from the PEER dataset.

significantly enhancing the robustness and reproducibility of the power spectral model estimates.

In summary, the data preprocessing ensured that power spectral calculations for all records were performed within the reliable frequency range, avoiding systematic biases caused by low- or high-frequency outliers. The processed signals effectively suppressed low-frequency drifts and high-frequency random noise while preserving the main waveform characteristics, resulting in power spectra with significantly converged mean and variance and more stable spectral shapes. This provides a robust and reliable data foundation for subsequent model development and parameter fitting across different magnitude-distance categories.

4. Bedrock power spectral model

4.1. Effects of magnitude and distance on the bedrock power spectrum

To further investigate the effects of magnitude and distance on the bedrock power spectrum, this section calculates the power spectrum of each bedrock seismic record selected in Section 3. The power spectrum can be obtained from the FAS using the following equation:

$$S(\omega) = \frac{F(\omega)^2}{T} \tag{14}$$

where $F(\omega)$ is the FAS; T is the duration of the strong seismic motion.

To calculate the FAS, the Fourier transform should first be applied to each selected bedrock seismic record to obtain the corresponding amplitude spectrum. Then, the moving average method was used to smooth each FAS, with a window size value of 20 [49]. In addition, accurately defining the duration of strong seismic motion is also essential for calculating the power spectrum. The energy duration is the most commonly utilized among various existing definitions, which contains 90 %, 80 % and 70 % energy of the whole seismic record [50–52]. In this section, the 90 % energy duration is applied.

Based on Eq. (14), bedrock power spectral curves were calculated for each ground motion record from the two datasets within each magnitude-distance category, and the average power spectrum was subsequently computed, which is presented in Figs. 6 and 7. It can be observed that the power spectrum exhibits pronounced systematic variations across the entire period range, indicating that bedrock seismic motions do not behave as white-noise processes but instead possess distinct spectral structures and energy distribution characteristics. Under different magnitude and distance conditions, the power spectral curves show systematic differences in amplitude, spectral shape, and low-frequency energy distribution, reflecting the combined effects of source characteristics and propagation path. To further illustrate the statistical variability of the power spectrum under different magnitude-distance conditions, 95 % confidence intervals were provided for each category to provide the dispersion among the samples.

As observed from Fig. 6, the magnitude-based classification results indicate that, under the same distance condition, the overall amplitude of the power spectrum increases significantly with increasing earthquake magnitude, particularly in the low-frequency range, where the spectral shape becomes flatter and broader. This trend suggests that larger-magnitude events release more energy and possess a higher proportion of low-frequency content, which can excite a wider range of effective frequencies. Meanwhile, the spectral peak shifts slightly toward lower frequencies, reflecting the influence of increased source dimensions and longer rupture durations on the distribution of low-frequency energy. Overall, increasing magnitude not only elevates the total energy level of the power spectrum but also expands the bandwidth of the low-frequency range, allowing bedrock ground motions to maintain higher energy over a broader period range.

From the distance-based classification results, under the same magnitude condition, the power spectral amplitude continuously decreases with increasing distance. Compared the variations with magnitude, the spectral bandwidth and dominant frequency remain largely stable and do not change significantly with distance. In addition to the overall reduction in power spectral amplitude, energy decay in the high-frequency range is particularly pronounced, resulting in a steeper decline in the high-frequency range of the spectrum. This indicates that,

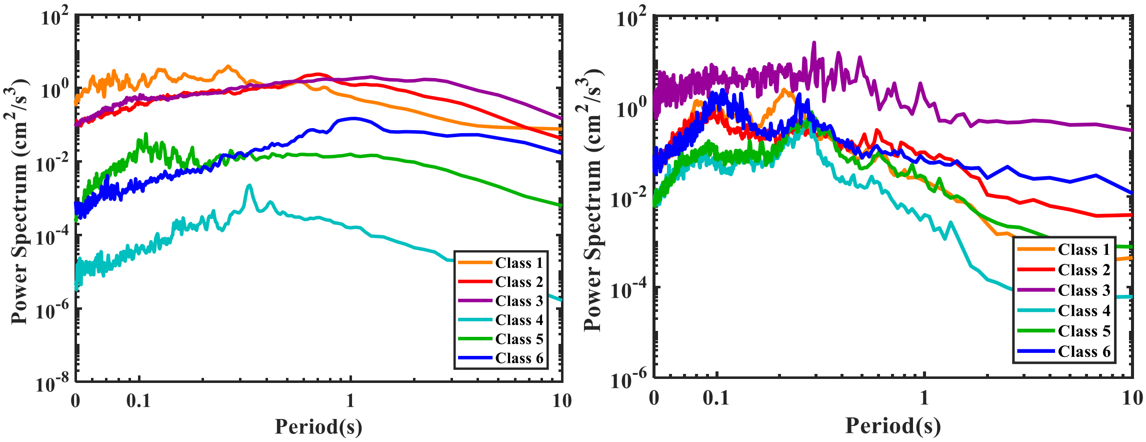

(a) K-NET and KiK-net dataset (b) PEER dataset

Fig. 8. Comparison of mean bedrock power spectrum under six classifications.

as distance increases, high-frequency components are more strongly attenuated due to the combined effects of geometric spreading and energy dissipation, while low-frequency energy remains relatively stable, leading to a low-frequency-dominated spectral distribution for far-field seismic motions.

The comprehensive analysis indicates that earthquake magnitude is the dominant factor controlling the power spectral amplitude and low-frequency bandwidth, while distance primarily governs the high-frequency energy attenuation. The combined effects of both magnitude and distance shape the typical spectral characteristics of bedrock seismic motions: near-field and large-magnitude events exhibit higher energy levels and broader low-frequency bands, whereas far-field and small-magnitude records are characterized by rapid high-frequency attenuation and overall reduced power spectral amplitudes.

As shown in Fig. 7, the bedrock power spectra across different magnitude-distance categories calculated from the PEER dataset exhibit overall patterns that are generally consistent with those derived from the K-NET and KiK-net, but with smoother spectral shapes, smaller amplitude variations, and relatively uniform energy distribution. Across different magnitude categories, the overall power spectral amplitude increases with magnitude, and the low-frequency bandwidth gradually expands, with spectral shapes becoming flatter. This indicates that larger-magnitude earthquakes can excite a broader frequency range, with more evenly distributed low-frequency energy and higher energy concentration. In addition, the spectral peak shifts slightly toward lower frequencies compared with smaller-magnitude events, suggesting that as magnitude increases, low-frequency components contribute more significantly during energy release, playing a more prominent role in long-period energy distribution.

Across different distance categories, the overall power spectral amplitude decreases with increasing distance, reflecting the typical attenuation effects during seismic wave propagation. Meanwhile, energy decay in the high-frequency range is particularly pronounced, resulting in a steeper decline in the high-frequency range of the spectrum, which indicates that high-frequency components are more strongly affected by geometric spreading and rapidly dissipate energy during propagation.

To provide a more intuitive illustration of the effects of magnitude and distance on bedrock power spectral characteristics, Fig. 8 presents a comprehensive comparison of the results. Within the same distance category, the overall power spectral amplitude increases with magnitude, and the decay in the high-frequency range becomes slower, resulting in a broader “effective bandwidth” for larger-magnitude earthquakes at the same frequency ranges. This is because the increase in magnitude lowers the corner frequency, reducing the high-frequency decay rate and extending the flat portion of the spectrum, allowing higher energy to be maintained in the high-frequency range. Conversely, within the same magnitude category, increasing distance leads to pronounced attenuation in the high-frequency portion of the power spectrum, accompanied by one or multiple oscillatory peaks. This behavior arises because greater distances enhance geometric spreading and energy dissipation effects, accelerating high-frequency decay and, in some cases, producing multiple peaks in the spectrum.

The consistency of results across the two datasets further validates the generality and reliability of the observed patterns, indicating that the influence of earthquake magnitude and distance on bedrock power spectrum exhibits stable statistical regularities. This provides a solid physical basis for the development of subsequent bedrock power spectral models and the estimation of their parameters.

4.2. Proposed bedrock power spectral model

Based on the bedrock power spectral results presented in the previous section, the spectral characteristics of bedrock seismic motions—including frequency content, amplitude, and bandwidth across different frequency ranges—are significantly influenced by earthquake magnitude and distance. Therefore, this section further examines the affection mechanisms caused by magnitude and distance, and proposes a bedrock power spectral model that explicitly accounts for both magnitude and distance through a statistical regression approach, based on the seismic records from the two datasets.

The power spectral curves generally exhibit a three-segment pattern consisting of a low-frequency range ($f < f_0$), a transition range ($f = f_0$), and a high-frequency range ($f > f_0$). In the low-frequency range, energy is primarily concentrated, and the spectrum is approximately flat; in the transition range, the spectrum begins to decay; and in the high-frequency range, the spectrum exhibits rapid attenuation. This behavior can be traced back to the source spectrum model proposed by Brune [45], in which the displacement amplitude spectrum, $S(f)$, is defined as:

$$S(f) = \frac{\Omega}{1 + (f/f_0)^2} \tag{15}$$

where Ω is the displacement spectral level corresponding to the low-frequency corner frequency f_0. The corresponding acceleration spectrum, $S_A(f)$, can then be obtained as:

$$S_A(f) = \frac{(2\pi f)^2 \Omega}{1 + (f/f_0)^2} \tag{16}$$

Eq. (16) can be rewritten as:

$$S_A(f) = 4\pi^2\Omega \times \frac{f^2}{1 + (f/f_0)^2} \tag{17}$$

where $4\pi^2\Omega$ can be regarded as the constant term corresponding to the source characteristics without affecting the frequency-dependent characteristics of the spectrum, while the fractional form $\frac{f^2}{1+(f/f_0)^2}$ controls the power spectral shape. To simultaneously account for the rising trend in the low-frequency range and the adjustable decay rate in the high-frequency range, the exponent in the denominator is generalized into an empirical form of γ, yielding the shape-controlling term, $H(f;f_0,\gamma)$, of the bedrock power spectral model:

$$H(f;f_0,\gamma) = \frac{f^{\ 2}}{1 + (f/f_0)^{\gamma}} \tag{18}$$

In the low-frequency range, the function is approximately proportional to $f^{\ 2}$, reflecting that the energy of seismic motion is primarily dominated by low frequencies. As the frequency approaches f_0, the attenuation trend gradually emerges. In the high-frequency range, the term $(f/f_0)^{\gamma}$ in the denominator controls the rapid decay rate of the power spectrum, where γ represents the high-frequency decay coefficient and serves as a key parameter determining the spectral shape. Compared with the fixed quadratic decay form in the Brune model, this exponential-type function allows for more flexible and accurate fitting of the spectral shape in the high-frequency range.

Based on the shape-controlling term, to further characterize the influence of magnitude and distance on the spectral properties, an amplitude-controlling term dominated by these two factors is considered. Most seismic motions adopt the moment magnitude M_w, which is related to the seismic moment M_0 as defined by the following relation:

$$M_w = \frac{2}{3}log_{10}M_0 - C' \tag{19}$$

where C' is a constant defined in different models. The seismic moment M_0 can be expressed as:

$$M_0 = 10^{1.5M_w + C} \tag{20}$$

where C is a constant. According to the source model proposed by Brune [45], the displacement spectral level Ω is proportional to the seismic moment, M_0:

$$\Omega \propto \frac{M_0}{4\pi\rho \upsilon^3 R} = \frac{10^{1.5M_w+C}}{4\pi\rho \upsilon^3 R} \tag{21}$$

where ρ denotes the medium density, and υ is the shear-wave velocity. By combining the constants and expressing them in the exponential form with base e, the spectral amplitude Ω is directly proportional to the moment magnitude:

$$\Omega \propto exp(1.5M_w + a) \tag{22}$$

where a is the constant which can be determined by fitting actual seismic motions.

Regarding the distance effects, based on the model proposed by Boore [35], the variation of spectral amplitude considers both geometric spreading and inelastic energy dissipation during propagation, and can be expressed as:

$$P(f,R) \propto \frac{1}{R} exp(\text{-}\pi f R \,/\, (Q(f\,)\cdot \upsilon)) \tag{23}$$

After averaging over the frequency effects, this exponential factor can be approximated as a power-law decay with distance, with the form of $1/R^{\beta}$, where β is a fitting parameter that accounts for both path attenuation and energy dissipation.

To provide a unified description of the combined effects of magnitude and distance on the overall power spectral amplitude, the two factors are integrated to construct an amplitude-controlling term, $\kappa(\theta)$:

$$\kappa(\theta) = \frac{exp(1.5M + a)}{\mathrm{b}R^{\beta}} \tag{24}$$

where M_w is abbreviated as M, representing the moment magnitude; b is the constant by fitting actual seismic motions.

In the equation, the magnitude term $exp(1.5M + a)$ originates from the exponential relationship between source radiated energy and magnitude, reflecting the exponential increase in energy release with magnitude. The distance decay term, $1/\mathrm{b}R^{\beta}$, represents geometric spreading and energy dissipation during wave propagation, causing the power spectral amplitude to gradually decrease with increasing distance.

Finally, considering the influence of noise or baseline drift in the low-frequency range, a low-frequency noise term c_0 is introduced, yielding the final bedrock power spectral model:

$$G(f) = \frac{exp(1.5M + a)}{\mathrm{b}R^{\beta}} \frac{f^{\ 2}}{1 + (f/f_0)^{\gamma}} + c_0 \tag{25}$$

The parameter vector is defined as $\theta = [a,\mathrm{b},\beta,f_0,\gamma,c_0]$. The proposed model is applicable for magnitude ranges of 4.8–8.2 and distances of 10–200 km, corresponding to the dataset used for regression. From Eq. (25), it can be seen that at zero frequency, the power spectral model satisfies the requirement of having no zero-frequency component. Meanwhile, as the frequency increases, the term $(f/f_0)^{\gamma}$ in the denominator causes the predicted spectrum to decay rapidly at high frequencies, ensuring that the total energy remains finite.

To further validate the physical plausibility of the proposed model, the influence mechanisms of magnitude and distance on the spectral shape were quantitatively investigated through the parametric formulation and fitting analysis of the power spectral model. Since the power spectral distributions across different magnitude and distance categories span several scale orders, direct fitting is susceptible to scale effects. Therefore, in this study, model parameters were estimated using a weighted least-squares approach in the logarithmic domain. The optimal parameter set $\widehat{\theta}$ was obtained by minimizing the weighted sum of squared residuals $J(\theta)$:

$$J(\theta) = \sum_f w(f)[\,y(f) - \widehat{y}(f\,;\,\theta)]^2 \tag{26}$$

where $y(f) = \log_{10}G_{obs}(f)$ the observed logarithmic power spectrum, $\widehat{y}(f;\ \theta) = \log_{10}(G\ (f;\ \theta) + \varepsilon)$ is the logarithmic power spectrum of the proposed model. $w(f)$ is the frequency weighting function, used to balance the contribution of different frequency ranges to the fitting.

Specifically, the weighting comprehensively accounts for the variance characteristics of the observed power spectra, the frequency-dependent SNR, and the physical reliability of the low-frequency range. First, the basic form of the weighting is defined based on the observed variance of the ground motion samples at each frequency point, so that frequency ranges with smaller variance and higher stability carry greater weight during fitting, thereby reducing the influence of high-noise intervals on parameter estimation. Second, considering that the high-frequency range is more susceptible to instrumental noise, the weight slightly decreases with increasing frequency to ensure fitting sensitivity in the mid- and low-frequency ranges. Meanwhile, the low-frequency range is appropriately up-weighted to enhance the model's ability to capture the corner frequency and spectral shape variations. Finally, all weights are normalized to ensure consistent dimensionality across different frequency ranges.

To quantitatively investigate the controlling mechanisms of magnitude and distance on the bedrock power spectral characteristics, the power spectra for different magnitude–distance categories were fitted to the proposed model, and the fitted parameters are presented in Tables 3

Table 3
Parameter fitting results of the K-NET and KiK-net dataset.

Distance (km)	Magnitude category	a	b	β	f_0	γ	c_0
$10 \leq R < 100$	$4.8 \leq M < 5.8$	3.69	1.65	1.26	5.12	3.72	1.0×10^{-8}
	$5.8 \leq M < 6.8$	6.65	0.95	1.28	5.07	3.41	0.005
	$6.8 \leq M < 8.2$	2.42	147.43	1.21	4.69	3.40	0.380
$100 \leq R \leq 200$	$4.8 \leq M < 5.8$	5.29	1.83	1.48	5.11	3.71	1.0×10^{-8}
	$5.8 \leq M < 6.8$	5.84	1.52	1.49	4.98	4.34	0.003
	$6.8 \leq M < 8.2$	2.32	166.73	1.28	4.89	3.76	0.006

Table 4
Parameter fitting results of the PEER dataset.

Distance (km)	Magnitude category	a	b	β	f_0	γ	c_0
$10 \leq R < 100$	$4.8 \leq M < 5.8$	2.22	13.64	1.23	3.09	3.13	0.011
	$5.8 \leq M < 6.8$	2.98	0.64	1.27	1.17	3.24	1.6×10^{-8}
	$6.8 \leq M < 8.2$	2.77	0.24	1.23	0.71	3.07	1.0×10^{-10}
$100 \leq R \leq 200$	$4.8 \leq M < 5.8$	5.73	20.07	1.53	2.58	4.32	1.0×10^{-8}
	$5.8 \leq M < 6.8$	5.12	1.57	1.46	1.19	3.26	9.0×10^{-5}
	$6.8 \leq M < 8.2$	3.91	0.78	1.36	0.54	3.76	1.0×10^{-8}

and 4. Specifically, with increasing earthquake magnitude, the fitted corner frequency f_0 systematically decreases, while the high-frequency decay coefficient γ slightly decreases. Physically, this reflects that larger earthquakes generate more low-frequency energy and longer rupture durations, which reduce the spectral roll-off and extend the flat portion of the spectrum. Conversely, for the same magnitude category, as distance increases, both γ and β exhibit an increasing trend, indicating stronger geometric spreading and energy dissipation effects during wave propagation, which accelerate the decay of high-frequency energy. These parameterized trends quantitatively confirm the variations previously observed in the power spectral curves, thereby linking the observed spectral features to underlying physical mechanisms of source and propagation effects. This combined numerical and physical analysis not only clarifies the sensitivity of the model parameters to key seismic inputs but also provides a robust basis for practical application and further refinement of the proposed model.

Finally, the fitting performance of the proposed model was evaluated using the weighted root-mean-square error (RMSE) and the weighted coefficient of determination (R^2) in the logarithmic domain. The RMSE is defined as:

$$\mathrm{RMSE} = \sqrt{\frac{1}{N_f}\sum_{f \in F}\left[y(f) - \hat{y}(f\,;\,\theta)\right]^2} \tag{27}$$

where N_f denotes the total number of frequency points used during the fitting. The determination weighted coefficient R^2 is defined as:

$$SS_{res} = \sum_{f}\left[\sqrt{w(f)} \times \left(y(f) - \hat{y}(f\,;\,\theta)\right)\right]^2 \tag{28}$$

$$SS_{\mathrm{tot}} = \sum_{f}\left[\sqrt{w(f)} \times \left(y(f) - \bar{y}(f)\right)\right]^2 \tag{29}$$

$$R^2 = 1 - \frac{SS_{res}}{SS_{\mathrm{tot}}} \tag{30}$$

where $\bar{y}(f)$ represents the weighted mean of the observed spectrum.

To further assess the reliability of the model fit to the observed power spectra, after obtaining the optimal parameter vector $\hat{\theta}$, the residual vector and its unbiased standard deviation are defined as follows:

$$e(f) = y(f) - \hat{y}(f\,;\,\hat{\theta}) \tag{31}$$

$$\hat{\sigma}_{res} = \sqrt{\frac{\sum_f e(f)^2}{N_f - p}} \tag{32}$$

where p denotes the number of fitted parameters and is used for degrees-of-freedom correction. This residual standard deviation can also serve as a quantitative indicator of the model's predictive uncertainty.

Assuming that the residuals follow a normal distribution, the 95 % confidence interval of the logarithmic observed power spectrum can be expressed as:

$$\mathrm{CI}_{95\%}(f) = y(f) \pm 1.96\sigma \tag{33}$$

where σ is the standard deviation of observed samples. This confidence interval characterizes the statistical uncertainty of the model at different frequency points and provides a basis for evaluating whether the predicted results fall within a reasonable statistical range and thereby evaluating the overall reliability and robustness of the model from the frequency-domain perspective.

Different from the conventional EPSD models, which primarily rely on empirical envelope functions to describe the temporal evolution of ground motion energy, the proposed model introduces two physical parameters—magnitude and distance—that simultaneously control the amplitude and shape of the power spectrum. This directly links the spectral characteristics to the physical mechanisms of source scaling and propagation path, rather than relying solely on statistical fitting. Specifically, existing EPSD models typically assume that the spectral shape of ground motion remains essentially constant over time; while they can capture the temporal decay of energy, they fail to represent the low-frequency bandwidth expansion associated with increasing magnitude or the rapid high-frequency energy decay induced by greater distance. In contrast, the present model is constructed based on a parametric frequency-domain formulation, using an amplitude-controlling term derived from magnitude and distance to represent source and path attenuation effects, while shape parameters such as β, f_0, and γ jointly determine the spectral form. By quantitatively linking these parameters to underlying physical mechanisms, the method not only more accurately captures the non-stationary evolution of seismic motion frequency content and energy distribution, but also enhances spectral shape fitting through an adjustable high-frequency decay term. Consequently, it significantly improves the fitting accuracy and generalizability of the model across different earthquake event scales and non-stationary characteristics.

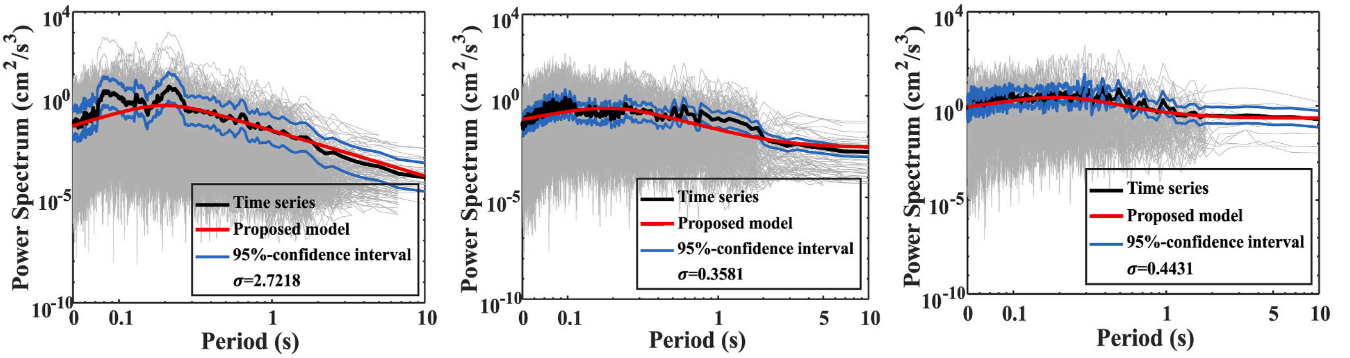

(a) $4.8 \le M < 5.8$, $10\text{km} \le R < 100\text{km}$ (b) $5.8 \le M < 6.8$, $10\text{km} \le R < 100\text{km}$ (c) $6.8 \le M < 8.2$, $10\text{km} \le R < 100\text{km}$

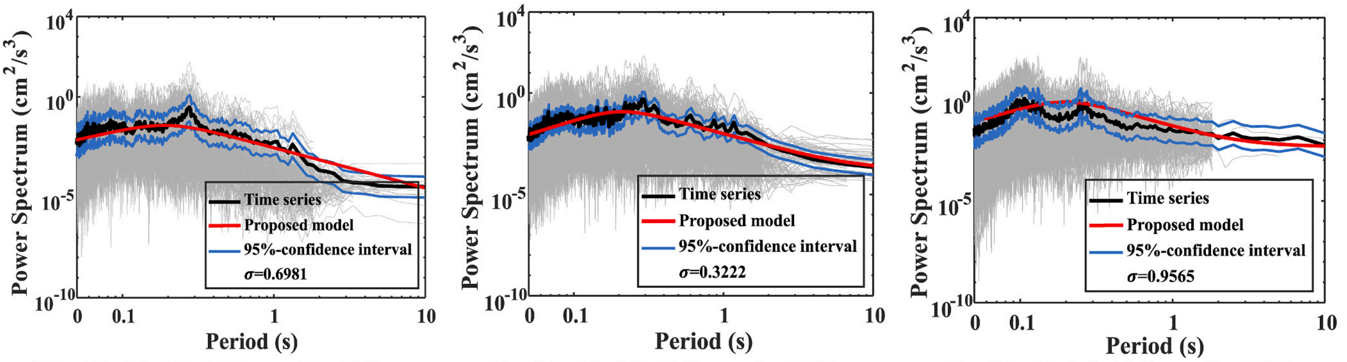

(d) $4.8 \le M < 5.8$, $100\text{km} \le R < 200\text{km}$ (e) $5.8 \le M < 6.8$, $100\text{km} \le R < 200\text{km}$ (f) $6.8 \le M < 8.2$, $100\text{km} \le R < 200\text{km}$

Fig. 9. Comparison results of the bedrock power spectrum of the proposed model and actual seismic records in Case 1.

4.3. Model validation and quantitative evaluation

4.3.1. Case 1: Validation results of K-NET and KiK-net dataset

The proposed bedrock power spectral model was validated using the seismic records from the K-NET and KiK-net datasets classified in Table 1, as shown in Fig. 9. For each magnitude-distance category, the power spectrum of each record and the corresponding mean result were first computed, represented by gray and black curves, respectively. Then, based on the magnitude and distance of each record, the model-predicted mean power spectrum was calculated and displayed as the red curve. To illustrate the predictive accuracy of the model, the 95 % confidence intervals of observed power spectral curves were also plotted, shown as blue curves.

For near-field earthquakes (10 km $\le R <$ 100 km), the model-predicted power spectrum generally agrees well with the average power spectrum computed from the seismic records. This agreement is particularly notable for moderate- ($5.8 \le M < 6.8$) and large-magnitude ($6.8 \le M < 8.2$), where the predicted curves largely fall within the 95 % confidence intervals, effectively reproducing the overall amplitude and frequency distribution of the power spectrum. However, for smaller magnitudes ($4.8 \le M < 5.8$), the model slightly underestimates the amplitude in the short-period range. In particular, when the observed power spectrum exhibits multiple local peaks, the predicted curves may slightly exceed the confidence intervals, indicating some deviation in reproducing local high-frequency details, while the overall trend remains well captured.

For far-field earthquakes (100 km $\le R <$ 200 km), the model predictions are generally consistent with the observed trends, with the predicted curves falling within the 95 % confidence intervals over most of the frequency range, accurately reflecting the attenuation of the spectrum with distance. However, the observed power spectrum occasionally exhibits multiple peaks in the high-frequency range, indicating complex mechanisms such as local path effects and specific disturbances. In these cases, the predicted curves may slightly exceed the confidence intervals, but the model still captures the main spectral shape and high-frequency decay trend effectively.

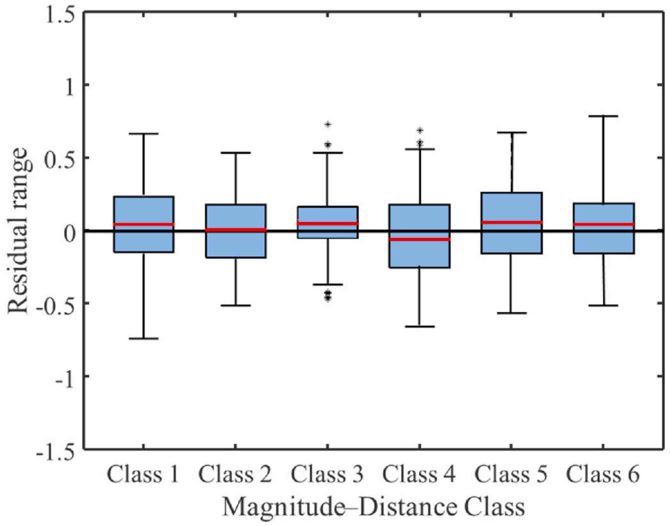

Fig. 10. Boxplot of power spectral residuals of six classifications in Case 1.

Overall, the proposed model can reliably reproduce the main features of the power spectra across different magnitude and distance conditions, including amplitude, bandwidth, and high-frequency decay trends. For both near-field and far-field categories, the majority of the model-predicted curves fall within the 95 % confidence intervals, demonstrating high predictive accuracy for the overall spectral trend and frequency-dependent attenuation. However, some deviations remain in capturing local high-frequency multi-peak features, particularly for smaller magnitudes ($4.8 \le M < 5.8$), providing a reference for

Table 5
Evaluation indicators in Case 1.

Distance (km)	Magnitude category	Class	RMSE	R^2	$\widehat{\sigma}_{res}$
$10 \le R < 100$	$4.8 \le M < 5.8$	1	0.3911	0.8404	0.3941
	$5.8 \le M < 6.8$	2	0.2526	0.9054	0.2545
	$6.8 \le M < 8.2$	3	0.2173	0.9287	0.2189
$100 \le R \le 200$	$4.8 \le M < 5.8$	4	0.2821	0.7971	0.2842
	$5.8 \le M < 6.8$	5	0.2440	0.8277	0.2459
	$6.8 \le M < 8.2$	6	0.3226	0.7154	0.3250

subsequent high-frequency corrections and multi-peak fitting.

To quantitatively evaluate the fitting accuracy of the proposed model, the RMSE, R^2, residuals, and residual standard deviation $\widehat{\sigma}_{res}$ were calculated for each category. Residuals were computed in the logarithmic domain and defined as the difference between the observed and model-predicted power spectrum, while the unbiased estimate of the residual standard deviation $\widehat{\sigma}_{res}$ was used to quantify the predictive uncertainty of the model. Fig. 10 presents the residual distributions as boxplots, providing a visual representation of the fitting errors across different magnitude-distance categories. The results indicate that residuals in each category are generally symmetrically distributed with medians close to zero (red line), suggesting no significant systematic bias in the model predictions. Overall, most residuals lie within the range of ±0.5, and the moderate box heights indicate small differences between predicted and observed values. Among them, Class 3 (larger-magnitude and near-field events) exhibits the most concentrated residuals with minimal variability, reflecting the best predictive performance. The other categories show similar residual concentration, but Class 1 (smaller-magnitude and near-field events) and Class 6 (larger magnitude and far-field events) have the largest interquartile ranges, indicating slightly higher predictive uncertainty in these two categories. This phenomenon may be related to the presence of high-frequency multi-peak features in the observed power spectra of these categories, which limits the model accuracy in reproducing local high-frequency details.

Furthermore, Table 5 summarizes the quantitative indicators RMSE, R^2, and $\widehat{\sigma}_{res}$ to compare the overall fitting performance of the proposed model across different classifications. The results show that Class 3 (larger-magnitude and near-field events) exhibits the smallest RMSE and $\widehat{\sigma}_{res}$ values and the highest R^2, indicating that the model achieves the most stable and reliable predictions in this category. In contrast, Class 1 (smaller-magnitude and near-field events) and Class 6 (larger-magnitude and far-field events) display relatively higher RMSE and $\widehat{\sigma}_{res}$ values and slightly lower R^2, suggesting greater bias and uncertainty in these predictions. Overall, the proposed model demonstrates strong capability in capturing the spectral characteristics and energy distribution of the power spectra under different magnitude-distance categories, with minor limitations observed primarily in high-frequency bands exhibiting complex multi-peak patterns.

4.3.2. *Case 2: Validation results of the PEER dataset*

To further evaluate the generalizability of the proposed model, seismic records from the PEER dataset were used for validation, and the results are presented in Fig. 11. Overall, the model successfully reproduces both the amplitude and frequency distribution characteristics of the power spectra under various magnitude and distance conditions. For near-field events (10 km $\le R <$ 100 km), the predicted spectra closely match the observed power spectra and fall within the 95 % confidence intervals in most frequencies. The best agreement is observed for moderate- ($5.8 \le M < 6.8$) and large-magnitude ($6.8 \le M < 8.2$) events. In contrast, for small-magnitude events ($4.8 \le M < 5.8$), the predicted spectra slightly exceed the confidence interval in local high-frequency ranges with pronounced fluctuations. For far-field events (100 km $\le R <$ 200 km), the predicted spectra generally follow the observed trends, successfully capturing the high-frequency attenuation characteristics. However, for moderate-magnitude events ($5.8 \le M <$ 6.8), noticeable fluctuations in the observed high-frequency amplitudes lead to slight exceedances of the confidence interval, which may be

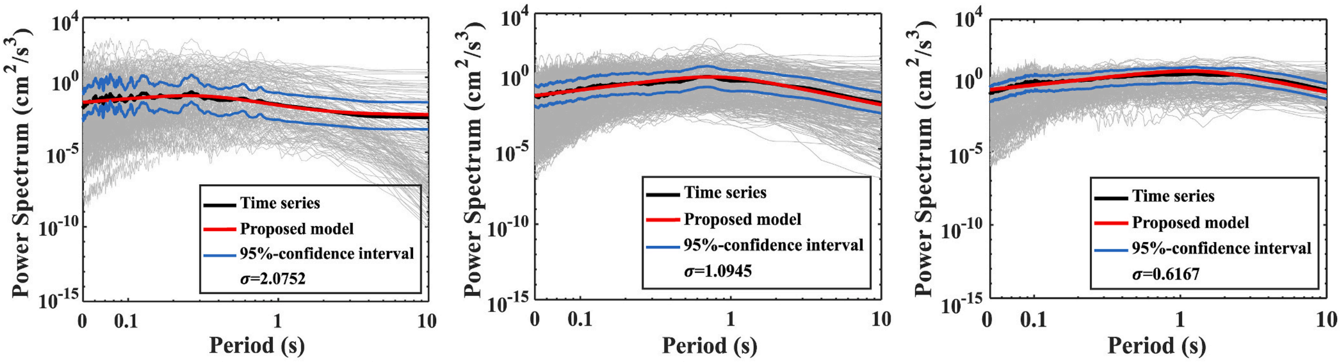

(a) 4.8≤M<5.8, 10km ≤ R < 100km (b) 5.8≤M<6.8, 10km ≤ R < 100km (c) 6.8≤M<8.2, 10km ≤ R < 100km

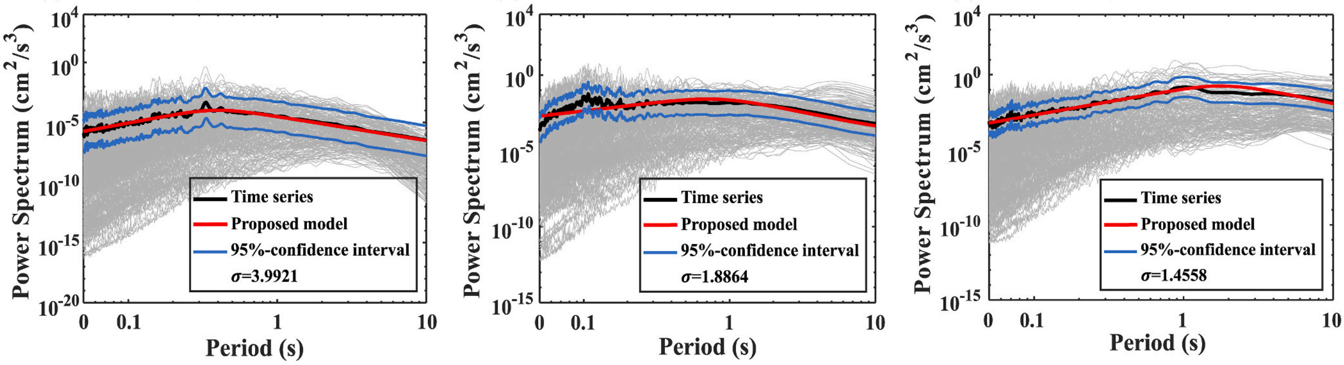

(d) 4.8≤M<5.8, 100km ≤ R < 200km (e) 5.8≤M<6.8, 100km ≤ R < 200km (f) 6.8≤M<8.2, 100km ≤ R < 200km

Fig. 11. Comparison results of the bedrock power spectrum of the proposed model and actual seismic records in Case 2.

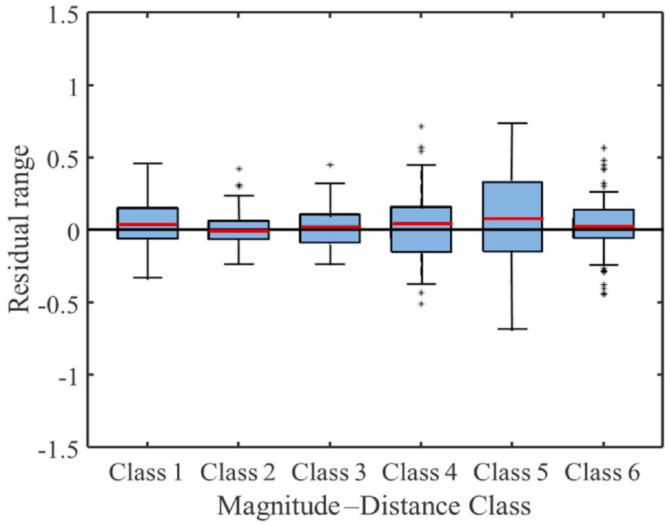

Fig. 12. Boxplot of power spectral residuals of six classifications in Case 2.

Table 6
Evaluation indicators in Case 2.

Distance (km)	Magnitude category	Class	RMSE	R^2	$\widehat{\sigma}_{res}$
$10 \le R < 100$	$4.8 \le M < 5.8$	1	0.1576	0.9100	0.1588
	$5.8 \le M < 6.8$	2	0.1030	0.9447	0.1038
	$6.8 \le M < 8.2$	3	0.1314	0.9700	0.1324
$100 \le R \le 200$	$4.8 \le M < 5.8$	4	0.1861	0.9110	0.1874
	$5.8 \le M < 6.8$	5	0.3978	0.8013	0.2308
	$6.8 \le M < 8.2$	6	0.1357	0.9007	0.1367

attributed to complex path effects.

Fig. 12 presents the boxplots of residuals for each classification. The results show that the residuals exhibit an overall symmetric distribution, with median values (red lines) close to zero, indicating the absence of significant systematic bias in the model predictions. In general, the residuals of all classifications are concentrated within the ±0.5 range, suggesting that the discrepancies between the predicted and observed power spectra are generally small. More specifically, the residuals for most classifications are concentrated and distributed with limited variability, demonstrating the robustness and reliability of the model predictions. In contrast, Class 5 (moderate-magnitude and far-field events) exhibits a relatively larger interquartile range, indicating higher deviations in this category. This may be attributed to the rapid high-frequency attenuation and noticeable fluctuations observed in the actual power spectra for this class.

Table 6 summarizes the RMSE, R^2, and $\widehat{\sigma}_{res}$ values under the PEER dataset. It can be observed that for near-field earthquakes (10 km $\le R <$ 100 km), the model exhibits relatively small RMSE and $\widehat{\sigma}_{res}$ values together with high R^2 values, indicating stable and reliable prediction performance within this range. For far-field earthquakes (100 km $\le R <$ 200 km), the model maintains a high level of predictive accuracy. However, Class 5 (moderate-magnitude and far-field events) shows relatively larger RMSE and $\widehat{\sigma}_{res}$ and a slightly lower R^2, suggesting the presence of certain prediction deviations and uncertainties. This may be attributed to the model's limited ability to capture multi-peak distributions and amplitude fluctuations in the high-frequency range, implying that further refinement is possible for this specific category.

4.4. Parameter study of the proposed bedrock power spectral model

In this section, a parameter sensitivity analysis of the proposed bedrock power spectral model is conducted. The calculations consider a range of earthquake magnitudes from 4.8 to 8.2 and distances from 10 km to 200 km, to investigate the influence of magnitude and distance on the characteristics of the power spectrum and to explore the underlying physical mechanisms.

Fig. 13 presents the model results for distances of 10 km, 50 km, 100 km, and 150 km under different magnitudes. It can be clearly observed that, for the same distance, the overall amplitude of the bedrock power spectrum increases significantly with increasing magnitude. This can be attributed to the higher seismic energy release of large-magnitude events, which more strongly excites energy in both the low- and mid-frequency ranges, thereby increasing the spectral amplitude. In addition, larger magnitudes lead to a flatter spectral curve in the low-frequency range and a wider bandwidth, indicating that large earthquakes are capable of exciting seismic waves over a broader frequency range with a more balanced energy distribution. This is because an increase in magnitude lowers the corner frequency, reduces the high-frequency attenuation rate, and extends the flat portion of the spectrum. This trend is highly consistent with the statistical patterns of actual seismic records, demonstrating that the model effectively captures the magnitude effect with strong physical plausibility.

Fig. 14 shows the model results for magnitudes of 5.0, 6.0, 7.0, and 8.0 under different distances. The results indicate that, under different magnitude conditions, distance has a relatively limited effect on the bandwidth of the power spectrum, which is primarily controlled by the source size and rupture duration. Within the same magnitude category, as the distance increases, the high-frequency portion of the power spectrum exhibits more pronounced attenuation, reflecting the effects of geometric spreading and energy dissipation during seismic wave propagation. Overall, the patterns presented in the figure demonstrate that distance exerts a significant influence on the overall amplitude decay and high-frequency energy distribution of the spectrum. These observed trends are in close agreement with the statistical results of actual bedrock seismic records, further validating the accuracy and applicability of the proposed model in representing both magnitude-dependent effects and distance attenuation characteristics.

Based on the proposed bedrock power spectral model, the Kanai-Tajimi model is combined to calculate the ground-surface power spectrum considering the effects of magnitude and distance. The spectral intensity factor S_0 of the white noise in the Kanai-Tajimi model is replaced by the proposed model $G(\omega)$. Then, the ground-surface power spectrum, considering the effects of magnitude and distance, named the

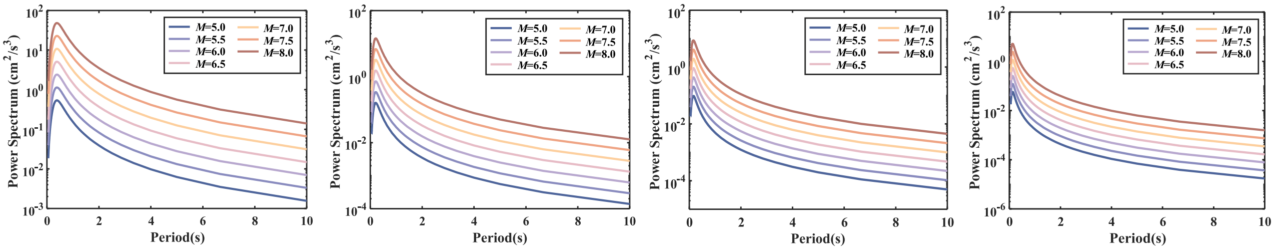

(a) $R = 10$km (b) $R = 50$km (c) $R = 100$km (d) $R = 150$km

Fig. 13. Results of the proposed bedrock power spectral model with different distances.

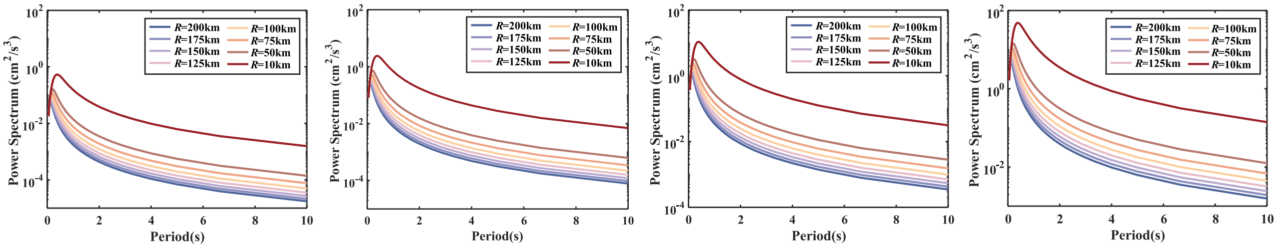

(a) $M = 5.0$ (b) $M = 6.0$ (c) $M = 7.0$ (d) $M = 8.0$

Fig. 14. Results of the proposed bedrock power spectral model with different magnitudes.

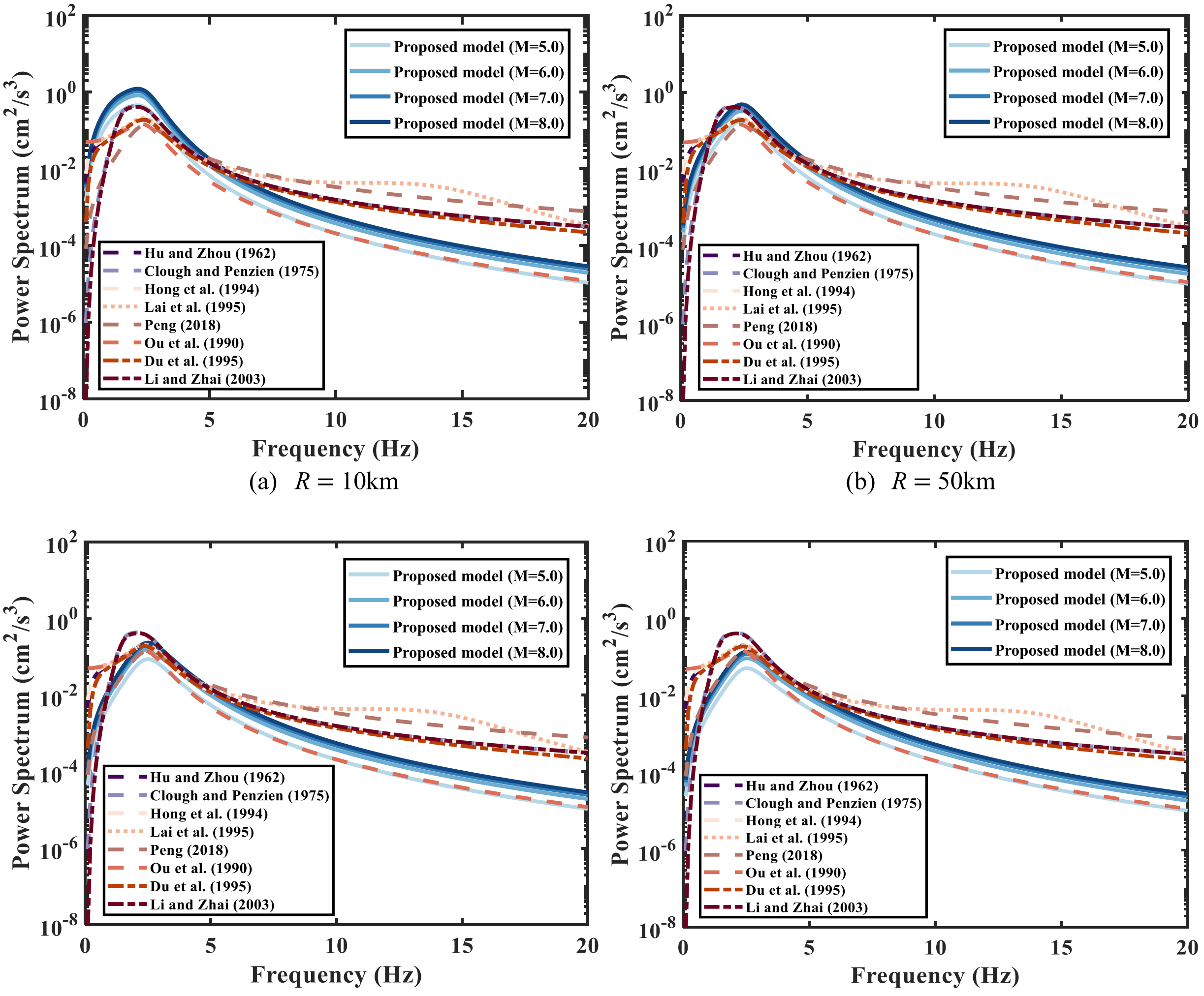

(a) $R = 10$km (b) $R = 50$km (c) $R = 100$km (d) $R = 150$km

Fig. 15. Comparison of the proposed model and other existing models.

modified Kanai-Tajimi model, can be expressed as follows:

$$G_s(\omega)=\frac{4\zeta_g{}^2\omega^2\omega_g{}^2+\omega_g{}^4}{4\zeta_g{}^2\omega^2\omega_g{}^2+\left(\omega_g{}^2\text{-}\omega^2\right)^2}G(\omega) \tag{34}$$

To further validate the universality of the proposed model, the spectral intensity factor S_0 in the stationary seismic models reviewed in Section 2.1 was replaced by the proposed model. Wherein, the ω_g and ζ_g are set as the same values to ensure that the comparison results are obtained under identical conditions. Then, the ground-surface power spectral results for several different magnitude and distance values were calculated and illustrated in Fig. 15. It can be observed that the power spectra computed using traditional models, which assume a constant bedrock power spectrum, exhibit a fixed shape that does not vary with frequency. In contrast, the improved model, which accounts for seismic magnitude and distance, produces surface power spectra that show significant variations in both amplitude and frequency distribution. Specifically, as the magnitude increases, the overall amplitude of the power spectrum rises markedly, and its flat plateau extends over a broader low-to-mid frequency range, reflecting stronger accumulation of seismic energy and wider frequency coverage. Conversely, as the distance increases, the attenuation in the high-frequency range becomes more pronounced, highlighting the influence of path effects on the seismic spectral characteristics. Compared with traditional models, the

Table 7
Error metrics for pulse-like and non-pulse-like groups.

Dataset	Near-field group	RMSE	R^2	$\hat{\sigma}_{res}$
K-NET and KiK-net	Pulse-like	0.3287	0.8861	0.3011
	Non-pulse-like	0.2694	0.9370	0.2579
PEER	Pulse-like	0.1472	0.9025	0.1527
	Non-pulse-like	0.1173	0.9558	0.1146

proposed magnitude- and distance-dependent bedrock power spectral model more accurately captures these non-stationary features, enabling the simulated surface power spectra to realistically represent the variations in energy distribution under different seismic scenarios.

According to the results shown in Fig. 15, the proposed model not only strictly satisfies the physical constraints that the bedrock power spectral density is zero at zero frequency and possesses finite energy, but also ensures that the computed surface power spectral density retains these critical characteristics. In the high-frequency range, the power spectrum of the proposed model rapidly decays to zero, demonstrating favorable frequency response properties. Compared with previous approaches that modified the Kanai-Tajimi model by introducing complex filters, the proposed model utilizes a statistical regression method considering the underlying physical mechanism, thereby avoiding cumbersome model tuning processes and achieving a more concise and efficient power spectral density calculation.

This advantage not only enhances the computational stability and physical consistency of the model but also lays a solid foundation for subsequent structural response analyses based on the power spectrum. Particularly in structural safety assessment and reliability analysis, an accurate and physically consistent surface power spectrum serves as a key input for predicting structural dynamic responses. Consequently, the proposed model can more precisely capture seismic ground motion characteristics, improving the scientific rigor and reliability of seismic performance evaluations, and providing engineering practice with a more effective tool for seismic simulation and risk assessment.

4.5. Near-field pulses and localized site effects

To quantitatively evaluate the robustness of the proposed model under near-field conditions where strong velocity pulses and associated directional effects may occur, the multi-component pulse identification algorithm proposed by Shahi and Baker [53] was applied to the near-field records ($R < 100$ km) from both datasets. Specifically, the two orthogonal horizontal components are analyzed using the CWT to identify the direction of the strongest pulse, based on which the records are classified into pulse-like and non-pulse-like groups. As summarized in Table 7, the pulse-like group exhibits larger RMSE and $\hat{\sigma}_{res}$ and a lower R^2 in the log-domain spectral fitting, indicating that the strong nonstationary and long-period energy concentration associated with pulse-dominated motions increases the difficulty of accurately reproducing detailed spectral features. Nevertheless, the overall spectral shape and primary attenuation trend of both groups are still captured consistently, suggesting that the proposed model remains reasonably robust in near-field conditions in terms of describing the overall energy-distribution pattern.

It should be noted that this experiment mainly classifies near-field records primarily based on whether a dominant velocity pulse is present. For more complex cases involving multiple pulses and composite pulse effects, the dispersion of fitting errors may further increase, particularly in the low-frequency range and around local spectral peaks. This limitation is consistent with the fact that a power spectral model characterizes energy distribution in the frequency domain but does not explicitly represent phase information or the time-varying envelope evolution of the motion.

With respect to localized site effects, the present model is intended to provide a parametric representation of the bedrock power spectrum governed by earthquake magnitude and distance, and the use of hard-rock records is designed to minimize shallow-layer amplification as much as possible. Consequently, localized site effects arising from strongly heterogeneous near-surface structures, lateral variations, and scattering are not explicitly incorporated in the proposed model. To extend the model to surface-spectral characterization for soft-soil sites or highly heterogeneous shallow layers, the proposed bedrock spectral model should be coupled with an appropriate site-response mechanism, such as a one-dimensional equivalent-linear site transfer function or a parameterized stochastic site model. Therefore, the proposed model is more suitable as a bedrock-input component to be used jointly with site models in surface spectral estimation or structural response analyses.

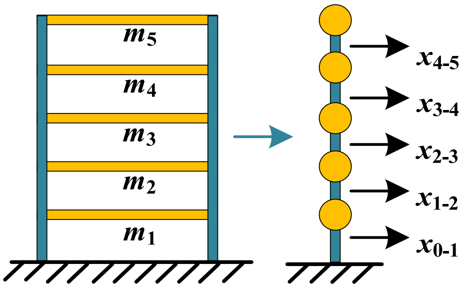

Fig. 16. Schematic diagram of a five-story structure.

Table 8
Structural responses of the traditional Kanai-Tajimi model.

Inter-story	Maximum inter-story relative displacement (cm)
0–1	0.9604
1–2	0.8273
2–3	0.8704
3–4	0.8263
4–5	0.9281
Max value	0.9604
P_S	100 %

4.6. Numerical example

To verify the effectiveness and engineering applicability of the proposed model in structural response analysis, a typical five-story linear-elastic frame structure is selected as a case study. The structure is modeled using a lumped-mass system, where the mass of each floor is idealized as a single concentrated mass point, allowing for a clearer representation of the structural dynamic response characteristics under seismic excitation. The simplified structural model is illustrated in Fig. 16. The structural response is evaluated in terms of the inter-story displacement, with the maximum inter-story displacement used to assess the overall deformation performance of the structure. In accordance with the corresponding threshold defined in current seismic design codes, the case with inter-story displacement exceeding this threshold is regarded as structural failure.

Taking the Kanai-Tajimi model as an example, this section uses both the traditional model and the modified Kanai-Tajimi model, provided in Eq. (34), which considers the effects of magnitude and distance to generate 10,000 synthetic seismic motions for structural analysis. The structural inter-story displacement responses and corresponding failure probabilities, P_S, are calculated and summarized in Tables 8 and 9. The results show that the proposed modified Kanai-Tajimi model can effectively predict the structural response characteristics under different magnitude and distance conditions. Specifically, the traditional Kanai-Tajimi model yields a maximum inter-story displacement of 0.9604 cm, with a structural failure probability of 100 %, indicating complete failure. In contrast, the modified Kanai-Tajimi model demonstrates physically reasonable variation trends of structural response. At the

Table 9
Structural responses of the modified Kanai-Tajimi model.

	Maximum inter-story relative displacement (cm)					
Inter-story	M = 5, R = 50 km	M = 5, R = 100 km	M = 5, R = 150 km	M = 6, R = 50 km	M = 6, R = 100 km	M = 6, R = 150 km
0–1	0.7325	0.4721	0.3581	0.9353	0.6354	0.4165
1–2	0.4713	0.2774	0.1939	0.5696	0.4137	0.2514
2–3	0.4668	0.2770	0.2236	0.5711	0.4165	0.2459
3–4	0.3942	0.3548	0.2170	0.5045	0.3838	0.2103
4–5	0.5249	0.2969	0.2016	0.6285	0.4685	0.2652
Max value	0.7325	0.4721	0.2259	0.9353	0.6454	0.4165
P_S	92.64 %	55.62 %	0. 01 %	100 %	57.21 %	0. 01 %
Inter-story	M = 7, R = 50 km	M = 7, R = 100 km	M = 7, R = 150 km	M = 8, R = 50 km	M = 8, R = 100 km	M = 8, R = 150 km
0–1	1.1657	0.6693	0.5137	1.3695	0.7263	0.5592
1–2	0.7387	0.4273	0.2898	0.7934	0.4793	0.3730
2–3	0.7107	0.4001	0.2752	0.7509	0.4936	0.3711
3–4	0.6263	0.3656	0.2489	0.6597	0.4273	0.3214
4–5	0.7640	0.4850	0.2850	0.7739	0.4973	0.3870
Max value	1.1657	0.6693	0.5137	1.3695	0.7263	0.5592
P_S	100 %	63.84 %	21.77 %	100 %	96.83 %	44.96 %

same magnitude ($M = 6$), the maximum inter-story displacement decreases significantly with increasing distance, from 0.9353 cm at $R = 50$ km to 0.4165 cm at $R = 150$ km. When the distance is the same ($R = 50$ km), the structural response increases with magnitude, from 0.7325 cm at $M = 5$ to 1.3695 cm at $M = 8$.

In terms of the failure probability, the modified Kanai–Tajimi model is capable of reflecting the combined effects of magnitude and distance on structural reliability. Specifically, for near-field earthquakes (10 km $\leq R < 100$ km), the failure probability of a large earthquake ($M = 8$, $R = 50$ km) approaches 100 %, consistent with the traditional model, indicating that structures generally reach or approach their ultimate state under large-magnitude and near-field events. In contrast, for far-field earthquakes (100 km $\leq R < 200$ km), the failure probability significantly decreases. For example, the failure probability in this category ($M = 8$, $R = 150$ km) is only 44.96 %. In this case, adopting a uniform assumption of 100 % failure probability based on near-field events would result in excessive safety margins and unnecessary material usage, reducing the economic efficiency of design. When the distance is the same, for instance, $R = 100$ km, as the magnitude increases from 5.0 to 8.0, the structural failure probabilities rise sequentially to 55.62 %, 57.21 %, 63.84 %, and 96.83 %, illustrating the dominant influence of magnitude on structural failure and highlighting the significant control of earthquake intensity on structural reliability. These results clearly demonstrate that structural safety varies considerably under different magnitude–distance combinations, whereas traditional models, which do not incorporate the physical constraints of magnitude and distance, tend to systematically overestimate the overall failure probability, masking the true safety levels of structures under different seismic scenarios.

Overall, the application of the proposed bedrock power spectral model that accounts for both magnitude and distance not only effectively differentiate structural response characteristics and failure probabilities under various seismic scenarios but also avoids the overly conservative design issues associated with traditional models relying on single-input assumptions. By regulating seismic energy and spectral distribution through magnitude and distance parameters, this model provides a power spectral representation with stronger physical-mechanism constraints and greater engineering applicability for structural reliability analysis and safety assessment.

5. Conclusions and future work

This study proposes a bedrock power spectral model that accounts for the effects of seismic magnitude and distance based on a statistical regression analysis of a large dataset of bedrock seismic records, effectively addressing the limitations of conventional models that assume bedrock motions behave as white noise. The model not only captures the variations of spectral amplitude, bandwidth, and high-frequency attenuation with magnitude and distance but also maintains a concise formulation that inherently satisfies the physical constraints of zero-frequency nullity and finite energy for both bedrock and surface spectra. By more accurately representing the time-frequency characteristics of seismic motions, the model significantly improves the precision of structural dynamic response predictions and provides a more physically consistent and accurate framework for structural reliability analysis and safety assessment.

Nevertheless, when multiple peaks appear in the high-frequency range, the model fitting accuracy may decrease. Future work will further refine the model to better represent high-frequency multi-peak spectra by introducing multi-peak spectral components or adopting frequency-band parameterization strategies, and will conduct systematic validation using a broader set of records and diverse structural case studies to examine its implications for reliability analysis and failure-probability assessment.

CRediT authorship contribution statement

Dengke Jiu: Writing – original draft, Visualization, Validation. **Yan-Gang Zhao:** Writing – review & editing, Funding acquisition. **Haizhong Zhang:** Supervision, Funding acquisition.

Declaration of competing interest

The authors declare that a similar paper is neither under consideration nor already published in another venue, and they have no known competing financial interests or personal relationships that could have appeared to influence the work reported in this paper.

Acknowledgments

This study was partially supported by the National Key R&D Program of China (Nos. 2023YFC3805100, 2023YFC3805101) and the Japan Society for the Promotion of Science (JSPS) KAKENHI (Grant No. 24K17336). This study used strong-motion records from K-NET and KiK-net databases. The authors are grateful for the financial supports and earthquake data.

Data availability

Data will be made available on request.

References

[1] Zhang X, Shen Y, Chang M, Su W, Tao W. Dynamic response and failure mode of a novel seismic structure for fault-crossing tunnel: theoretical analysis and shaking table test verification. Eng Fail Anal 2025;177:109671.

[2] Mohsenian V, Gharaei-Moghaddam N, Moghadam AS. Evaluation of slab–wall connections in tunnel form concrete structures: a multi-level approach based on seismic demand and capacity. Eng Fail Anal 2024;156:107833.

[3] Kim J, Kim T. Efficient seismic fragility analysis considering uncertainties in structural systems and ground motions. Earthq Eng Struct Dynam 2025;54:206–26.

[4] Zhang D-Y, Liu W, Xie W-C, Pandey MD. Modeling of spatially correlated, site-reflected, and nonstationary ground motions compatible with response spectrum. Soil Dynam Earthq Eng 2013;55:21–32.

[5] Zhang R, Huang D, Liu N, Jin F. Quantifying the effect of ground-motion nonstationarity on the nonlinear dynamic responses of an ultra-high arch dam. Soil Dynam Earthq Eng 2022;155:107194.

[6] Liu J, Meng X, Tian L, Jin Q, Dong Y, Yang M, Liu K. Failure mechanisms and seismic fragility analysis of overhead transmission lines incorporating pile-soil-structure interaction. Eng Fail Anal 2024;160:108201.

[7] Christian JT. Generating seismic design power spectral density functions. Earthq Spectra 1989;5:351–68.

[8] Ellingwood B, Maes M, Michael Bartlett F, Beck AT, Caprani C, Der Kiureghian A, Dueñas-Osorio L, Galvão N, Gilbert R, Li J, Matos J, Mori Y, Papaioannou I, Parades R, Straub D, Sudret B. Development of methods of structural reliability. Struct Saf 2025;113:102474.

[9] Wang D, Fan Z, Hao S, Zhao D. An evolutionary power spectrum model of fully nonstationary seismic ground motion. Soil Dynam Earthq Eng 2018;105:1–10.

[10] Chen B, Sun G, Li H. Power spectral models of stationary earthquake-induced ground motion process considering site characteristics. Emerg Manag SciTechnol 2022;2:1–12.

[11] Kanai K. 3. On the spectrum of strong earthquake motions, vol. 39; 1961. p. 85–95.

[12] Tajimi H. A statistical method of determining the maximum response of a building structure during an earthquake. In: Proc. of the 2nd world conference on earthquake engineering; 1960, 1960. p. 781–97. Tokyo, Japan.

[13] Clough R, Penzien J. Of structures. NY, USA: McGraw-Hill; 1975.

[14] Dai CY, Wang J. An improved Hu–Ou ground motion model. J Liaon Univ Eng Technol: Nat Sci Ed 2017;36:5.

[15] Kong C, Wang SG, Du DS, Li WW. Site-dependent ground motion power spectral model and parameter determination. Proceedings of the 23rd national academic conference on structural engineering, vol. III; 2014.

[16] Li YM, Liu LP, Lai M. Analysis and improvement of power random spectra of strong ground motions for engineering purpose, vol. 25. Gongcheng Lixue/Engineering Mechanics; 200843–48+57.

[17] Bittner M, Behrendt M, Beer M. Relaxed evolutionary power spectral density functions: a probabilistic approach to model uncertainties of non-stationary stochastic signals. Mech Syst Signal Process 2024;211:111210.

[18] Su H, Wang D, Xu S, Wang L, Zhu R. Exploring frequency-domain nonstationary of seismic ground motions using evolutionary power spectrum and Archimedean Copula functions. Soil Dynam Earthq Eng 2024;177:108364.

[19] Du A, Wang X, Xie Y, Dong Y. Regional seismic risk and resilience assessment: methodological development, applicability, and future research needs – an earthquake engineering perspective. Reliab Eng Syst Saf 2023;233:109104.

[20] Hong HP. On the estimation of the evolutionary power spectral density. Mech Syst Signal Process 2023;190:110131.

[21] Priestley MB. Power spectral analysis of non-stationary random processes. J Sound Vib 1967;6:86–97.

[22] Spanos Pol D, Failla G. Evolutionary Spectra estimation using wavelets. J Eng Mech 2004;130:952–60.

[23] Vlachos C, Papakonstantinou KG, Deodatis G. A multi-modal analytical non-stationary spectral model for characterization and stochastic simulation of earthquake ground motions. Soil Dynam Earthq Eng 2016;80:177–91.

[24] Hong-jing LI, Chen C. A modified Kanai-Tajimi spectral model for the stationary earthquake induced ground motion process. Eng Mech 2014;31:158–63.

[25] Ge X, Gong J, Zhao C, Azim I, Yang X, Li C. Structural dynamic responses of building structures with non-viscous dampers under Kanai–Tajimi spectrum excitation. J Sound Vib 2022;517:116556.

[26] Luis S. Predict the magnitudes of seismic events using Bayesian methods. Soil Dynam Earthq Eng 2020;129:105914.

[27] Lekić V, Matas J, Panning M, Romanowicz B. Measurement and implications of frequency dependence of attenuation. Earth Planet Sci Lett 2009;282:285–93.

[28] Wang G. A ground motion selection and modification method capturing response spectrum characteristics and variability of scenario earthquakes. Soil Dynam Earthq Eng 2011;31:611–25.

[29] Vlachos C, Papakonstantinou KG, Deodatis G. Predictive model for site specific simulation of ground motions based on earthquake scenarios. Earthq Eng Struct Dynam 2018;47:195–218.

[30] Bayless J, Abrahamson NA. Summary of the BA18 ground-motion model for fourier amplitude spectra for crustal earthquakes in California. 2019.

[31] Wang D, Fan Z, Hao S, Zhao DJSD, Engineering E. An evolutionary power spectrum model of fully nonstationary seismic ground motion, vol 105; 2018. p. 1–10.

[32] Ding J, Lu D, Cao Z. A hybrid non-parametric ground motion model of power spectral density based on machine learning. Comput Aided Civ Infrastruct Eng 2025;40:483–502.

[33] Luo C, Peng Y. Stochastic simulation of earthquake ground motions based on improved finite-fault model. Soil Dynam Earthq Eng 2024;176:108336.

[34] Wang J, Fan L, Qian S, Zhou J. Simulations of non-stationary frequency content and its importance to seismic assessment of structures. Earthq Eng Struct Dynam 2002;31:993–1005.

[35] Boore DM. Simulation of ground motion using the stochastic method. Pure Appl Geophys 2003;160:635–76.

[36] Chioccarelli E, Iervolino I. Near-source seismic hazard and design scenarios. Earthq Eng Struct Dynam 2013;42:603–22.

[37] Han R, Peng Y. An evolutionary power spectral density model for typical pulse-like ground motions in structural random vibration analysis. Mech Syst Signal Process 2025;237:113057.

[38] Bañales I, Christen JA, Tago J. Modeling evolutionary power spectral density functions of strong earthquakes via copulas. Soil Dynam Earthq Eng 2024;185:108859.

[39] Fang W, Cui X, Ji D, Zhai C. An efficient ground motion model coupling spatial correlations for large-scale field simulation. Soil Dynam Earthq Eng 2025;199:109696.

[40] Li M, Cui X. Time–frequency representation and spatial correlation model for ground motions with different fault mechanisms. ASCE-ASME J Risk Uncertainty Eng Syst, Part A: Civ Eng 2025;11:04025080.

[41] Cui XZ, Hong HP. A time–frequency representation model for seismic ground motions. Bull Seismol Soc Am 2020;111:839–56.

[42] Kanno T, Narita A, Morikawa N, Fujiwara H, Fukushima Y. A new attenuation relation for strong ground motion in Japan based on recorded data. Bull Seismol Soc Am 2006;96:879–97.

[43] Uchide T, Imanishi K. Underestimation of microearthquake size by the magnitude scale of the Japan meteorological agency: influence on earthquake statistics. Journal of Geophysical Research (Solid Earth) 2018;123:606–20.

[44] Thompson EM, Worden CB. Estimating rupture distances without a rupture. Bull Seismol Soc Am 2017;108:371–9.

[45] Brune JN. Tectonic stress and the spectra of seismic shear waves from earthquakes. Journal of Geophysical Research (1896-1977) 1970;75:4997–5009.

[46] Atkinson GM, Boore DM. Ground-motion relations for eastern North America. Bull Seismol Soc Am 1995;85:17–30.

[47] Kalkan E. An automatic P-Phase arrival-time picker. Bull Seismol Soc Am 2016;106:971–86.

[48] Bahrampouri M, Rodriguez-Marek A, Shahi S, Dawood H. An updated database for ground motion parameters for KiK-net records. Earthq Spectra 2021;37:505–22.

[49] Hu X, Hou J, Yin Y, Liu Y, Wang L, Kang Q, Hou M. A multi-scale blocking moving window algorithm for geostatistical seismic inversion. Comput Geosci 2023;173:105313.

[50] Trifunac MD, Brady AG. A study on the duration of strong earthquake ground motion. Bull Seismol Soc Am 1975;65:581–626.

[51] Bommer JJ, MartÍNez-Pereira A. The effective duration of earthquake strong motion. J Earthq Eng 1999;3:127–72.

[52] Taflampas IM, Spyrakos CC, Koutromanos IA. A new definition of strong motion duration and related parameters affecting the response of medium–long period structures. Soil Dynam Earthq Eng 2009;29:752–63.

[53] Shahi SK, Baker JW. An efficient algorithm to identify strong-velocity pulses in multicomponent ground motions. Bull Seismol Soc Am 2014;104:2456–66.